Available online at www.sciencedirect.com
ScienceDirect
Comput. Methods Appl. Mech. Engrg. 391 (2022) 114550
Computer methods in applied mechanics and engineering
www.elsevier.com/locate/cma

Maximum-principle-satisfying discontinuous Galerkin methods for incompressible two-phase immiscible flow

M.S. Joshaghani[a,*], B. Riviere[a], M. Sekachev[b]

[a] *Rice University, Houston, TX 77005, United States of America*
[b] *TotalEnergies, Houston, TX 77002, United States of America*

Received 22 June 2021; received in revised form 10 November 2021; accepted 26 December 2021
Available online 1 February 2022

Graphical Abstract

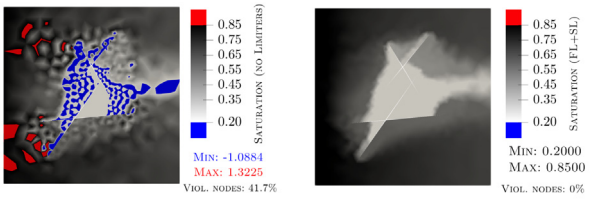

(a) DG with no limiters (b) DG scheme with proposed limiters; $t = 1000$ s

This figure shows the saturation profiles of a pressure-driven flow problem at time $t = 1000$ s. The porous medium is homogeneous and contains a thin barrier. Solutions are obtained using discontinuous Galerkin (DG) scheme without limiters (left) and with the proposed limiters (right). We observe that DG approximation with no limiter yields noticeable violations, while limited DG scheme is capable of providing maximum-principle satisfying results. The physical range for solutions is between s_{rw} and $1 - s_{r\ell}$ (between 0.2 and 0.85 in this problem); and is shown in grayscale. Values below and above bounds are colored blue and red, respectively.

Abstract

This paper proposes a fully implicit numerical scheme for immiscible incompressible two-phase flow in porous media taking into account gravity, capillary effects, and heterogeneity. The objective is to develop a fully implicit stable discontinuous Galerkin (DG) solver for this system that is accurate, bound-preserving, and locally mass conservative. To achieve this, we augment our DG formulation with post-processing flux and slope limiters. The proposed framework is applied to several benchmark problems and the discrete solutions are shown to be accurate, to satisfy the maximum principle and local mass conservation.

Keywords: Two-phase flow; Heterogeneous media; Discontinuous Galerkin; Gravity effect; Maximum-principle-satisfying method; Local mass conservation

* Corresponding author.
E-mail address: m.sarraf.j@rice.edu (M.S. Joshaghani).

https://doi.org/10.1016/j.cma.2021.114550
0045-7825/

1. Introduction

Multiphase flows in porous media appear in a large number of applications in engineering and sciences, for instance in the environmental clean up of contaminated subsurface or in the energy production of hydrocarbons from reservoirs. This paper introduces a numerical method for solving the immiscible two-phase flow equations, that produces bound-preserving discrete saturations. The proposed method utilizes a fully implicit in time stepping scheme, a discontinuous Galerkin in space discretization and post-processing flux and slope limiters techniques. The resulting numerical saturation is shown to satisfy a maximum principle theoretically and computationally.

The numerical literature for immiscible two-phase flow problems is vast (see [1–3] and references herein). Suitable numerical methods should be locally mass conservative and should produce bound-preserving discrete saturations. Such methods include finite difference methods and finite volume methods, which are popular methods because of their simplicity and low cost [4–6]. However, finite difference methods are not adapted to unstructured meshes and cell-centered finite volume methods suffer from grid distortion and do not easily handle full anisotropy. More recent methods that are locally mass conservative include the mixed finite element methods and multipoint flux methods [7–11]. The class of interior penalty discontinuous Galerkin methods has been applied to model multiphase flows in porous media for more than fifteen years [12–18] and they have been combined with other locally mass conservative methods like mixed finite element methods in [19,20]. DG methods are locally mass conservative, they do not suffer from grid distortion and they are accurate and robust even in the case of anisotropic heterogeneous media. However, it is well known that the DG approximation of the saturation does not satisfy a maximum principle because of local overshoots and undershoots in the neighborhood of the saturation front. While the amount of overshoot and undershoot can be reduced by the choice of implicit time stepping, mesh refinement and appropriate penalty parameters, there is no guarantee that they will completely disappear. The literature on post-processing techniques to reduce or eliminate the amount of overshoots and undershoots for DG methods in general is significant. Slope limiters adjust the gradient of the linear approximation in a heuristic way [21–26]. Recently, flux limiters related to flux-corrected transport algorithms, were introduced for DG discretizations of conservation laws [27,28].

The main contribution of this paper is the formulation of bound-preserving numerical method for the incompressible two-phase flow problems. Upwind fluxes are employed for the interior penalty discontinuous Galerkin discretization in space. We solve several benchmark problems to investigate the performance of the method and particularly the impact of the limiting techniques on local mass conservation. The numerical method respects maximum principle by limiting the saturation profile to physical upper- and lower-bounds. The violation of maximum principle for the discontinuous approximation of the saturation has been an open problem over the last decade. Our proposed scheme guarantees that the saturation remains bounded in the physical range. In addition, we observe that the monotonicity of the saturation is significantly improved compared to the case of no limiters. Saturation fronts are sharp with minimal numerical diffusion. We present several numerical results that show overshoots and undershoots have been eliminated. We verify that the local mass conservation property is also satisfied. We consider cases where flow is driven by boundary conditions and cases where flow is driven by injection and production wells. In the former case, a theoretical proof of the maximum principle is given.

The content of the paper is as follows. Section 2 describes the mathematical equations. The primary unknowns are the wetting phase pressure and saturation. Section 3 contains the fully implicit numerical scheme, with the construction and analysis of the flux limiters, and the review of slope limiters used in this work. Several numerical results, including benchmark problems and convergence tests, are given in Section 4. Conclusions follow.

2. Governing equations

The incompressible two-phase flow in a porous medium $\Omega \subset \mathbb{R}^2$ over a time interval $[0, T]$, is modeled by a system of mass balance equations for each phase, coupled with closure relations.

$$\frac{\partial}{\partial t}(\phi S_\alpha) - \nabla \cdot (\lambda_\alpha K(\nabla P_\alpha - \rho_\alpha \mathbf{g})) = q_\alpha, \quad \alpha = \ell, w, \tag{2.1}$$

$$S_\ell + S_w = 1, \tag{2.2}$$

$$P_c = P_\ell - P_w. \tag{2.3}$$

where P_w (resp. P_ℓ) is the wetting phase (resp. non-wetting phase) pressure and S_w (resp. S_ℓ) is the wetting phase (resp. non-wetting phase) saturation. The source/sink functions are denoted by q_α, the phase mobility coefficient by λ_α and the capillary pressure, P_c. The phase mobilities are ratios of the relative permeabilities, $k_{r\alpha}$, to the phase viscosities, μ_α. Relative permeabilities and capillary pressure are given functions of the wetting phase saturations [29].

$$\lambda_\alpha(S_w) = \frac{k_{r\alpha}(S_w)}{\mu_\alpha}, \quad \alpha = w, \ell. \tag{2.4}$$

The relative permeabilities may vanish at one endpoint of the saturation range; the exact expressions for $k_{r\alpha}$ are given for each numerical example in Section 4. We regularize the capillary pressure near the zero saturation by a linear approximation (see formula (4.8)). The other coefficients are the porosity ϕ, the absolute permeability K, and the gravity vector $\mathbf{g}$. Using (2.2) and (2.3), and choosing for primary unknowns the wetting phase pressure and saturation $(P, S) = (P_w, S_w)$, the system of equations reduces to:

$$\frac{\partial}{\partial t}\big(\phi(1-S)\big) - \nabla\cdot\Big(\lambda_\ell(S)K\big(\nabla P + \nabla P_c(S) - \rho_\ell \mathbf{g}\big)\Big) = q_\ell, \qquad \text{in } \Omega\times(0,T), \tag{2.5}$$

$$\frac{\partial}{\partial t}\big(\phi S\big) - \nabla\cdot\Big(\lambda_w(S)K\big(\nabla P - \rho_w \mathbf{g}\big)\Big) = q_w, \qquad \text{in } \Omega\times(0,T). \tag{2.6}$$

Let the boundary of the domain be divided into different disjoint sets

$$\partial\Omega = \Gamma^{\mathrm{D},p}\cup\Gamma^{\mathrm{N},p} = \Gamma^{\mathrm{D},s}\cup\Gamma^{\mathrm{N},s}\cup\Gamma^{\mathrm{out},s}.$$

Dirichlet and Neumann boundary conditions are imposed on parts of the boundary:

$$P = g^p, \qquad \text{on } \Gamma^{\mathrm{D},p}\times(0,T), \tag{2.7}$$

$$S = g^s, \qquad \text{on } \Gamma^{\mathrm{D},s}\times(0,T), \tag{2.8}$$

$$\lambda_\ell(S)K\big(\nabla P + \nabla P_c(S) - \rho_\ell\mathbf{g}\big)\cdot\mathbf{n} = j^p, \qquad \text{on } \Gamma^{\mathrm{N},p}\times(0,T), \tag{2.9}$$

$$\lambda_w(S)K\big(\nabla P - \rho_w\mathbf{g}\big)\cdot\mathbf{n} = j^s, \qquad \text{on } \Gamma^{\mathrm{N},s}\times(0,T). \tag{2.10}$$

The outflow boundary $\Gamma^{\mathrm{out},s}$ is a do-nothing boundary used in pressure-driven flow problems. This boundary is treated as an extension of interior facets in a sense that the surface integrals on this boundary are evaluated in terms of the unknown saturations. It should be noted that we did not incorporate non-reflecting conditions [30,31] or infinite edge elements [32] in our DG code and the name "outflow" used here should not be mixed up with the Lenzinger and Schweizer [33] outflow boundary at the interface of porous media and a free flow media.

In the case of pure homogeneous Neumann boundary conditions ($\Gamma^{\mathrm{N},s} = \Gamma^{\mathrm{N},p} = \partial\Omega$) and $j^p = j^s = 0$), the flow is driven by injection/production wells (source/sink functions) that depend on the wetting phase saturation as follows:

$$q_\alpha(S) = f_\alpha(s_{\mathrm{in}})\bar{q} - f_\alpha(S)\underline{q}, \quad \alpha = \ell, w.$$

The functions $\bar{q}$ and $\underline{q}$ correspond to the injection and production well rates and s_{in} is the prescribed wetting phase saturation at the injection wells. The fractional flow functions, f_α, are the ratios of the phase mobility to the total mobility, $f_\alpha = \lambda_\alpha/(\lambda_\ell + \lambda_w)$.

Finally the model problem is completed by an initial condition on the saturation: $S = s_0$. While our paper focuses on the numerical discretization of the equations above, existence of a weak solution was first done in [34,35].

3. Numerical method

The domain Ω is decomposed into a non-degenerate partition $\mathcal{E}_h = \{E\}_E$ consisting of N_h triangular or rectangular elements of maximum diameter h. Let Γ_h denote the set of all edges and Γ_h^i denote the set of interior edges. For any $e\in\Gamma_h^i$, fix a unit normal vector $\mathbf{n}_e$ and denote by E^+ and E^- the elements that share the edge e such that the vector $\mathbf{n}_e$ is directed from E^+ to E^-. We define the jump and average of a scalar function ξ on e as follows:

$$[\xi] = \xi|_{E^+} - \xi|_{E^-}, \quad \{\xi\} = \frac{1}{2}\left(\xi|_{E^+} + \xi|_{E^-}\right). \tag{3.1}$$

By convention, if e is adjacent to $\partial\Omega$, then the jump and average of ξ on e coincide with the trace of ξ on e and the normal vector $\mathbf{n}_e$ coincides with the outward normal $\mathbf{n}$. Let $\mathcal{P}_1(E) = \mathbb{P}_1(E)$ be the space of polynomials of total degree ≤ 1 if E is a simplex and let $\mathcal{P}_1(E) = \mathbb{Q}_1(E)$ be the space of polynomials of degree ≤ 1 in each variable. The discontinuous finite element space of order one is:

$$\mathcal{D}(\mathcal{E}_h) = \left\{\xi \in L^2(\Omega) : \xi|_E \in \mathcal{P}_1(E),\ \forall E \in \mathcal{E}_h\right\}. \tag{3.2}$$

The time interval T is divided into N_τ equal subintervals of length τ. Let P_n and S_n be the numerical solutions at time t_n. The proposed discontinuous Galerkin scheme for Eqs. (2.5)–(2.10) reads: Given $(P_n, S_n) \in \mathcal{D}(\mathcal{E}_h) \times \mathcal{D}(\mathcal{E}_h)$, find $(P_{n+1}, S_{n+1}) \in \mathcal{D}(\mathcal{E}_h) \times \mathcal{D}(\mathcal{E}_h)$ such that:

$$\begin{aligned}
&\frac{1}{\tau}\int_\Omega \phi(1-S_{n+1})\xi + \sum_{E\in\mathcal{E}_h}\int_E \lambda_\ell(S_{n+1})K\left(\nabla P_{n+1} + \nabla P_c(S_{n+1}) - \rho_\ell \mathbf{g}\right)\cdot\nabla\xi \\
&- \sum_{e\in\Gamma_h^i}\int_e (\lambda_\ell(S_{n+1}))^{\uparrow \mathbf{v}_\ell^n}\{K\left(\nabla P_{n+1} + \nabla P_c(S_{n+1}) - \rho_\ell \mathbf{g}\right)\cdot\mathbf{n}_e\}[\xi] \\
&- \sum_{e\in\Gamma^{\mathrm{D},p}}\int_e \lambda_\ell(S_{n+1})K\left(\nabla P_{n+1} + \nabla P_c(S_{n+1}) - \rho_\ell \mathbf{g}\right)\cdot\mathbf{n}_e\,\xi + \sum_{e\in\Gamma_h^i\cup\Gamma^{\mathrm{D},p}}\frac{\sigma}{h}\int_e [P_{n+1}][\xi] \\
&= \int_\Omega q_\ell(S_n)\xi + \frac{1}{\tau}\int_\Omega \phi(1-S_n)\xi + \frac{\sigma}{h}\int_{\Gamma^{\mathrm{D},p}} g^p\xi + \int_{\Gamma^{\mathrm{N},p}} j^p\xi, \quad \forall\xi\in\mathcal{D}(\mathcal{E}_h),
\end{aligned} \tag{3.3}$$

$$\begin{aligned}
&\frac{1}{\tau}\int_\Omega \phi S_{n+1}\xi + \sum_{E\in\mathcal{E}_h}\int_E \lambda_w(S_{n+1})K\left(\nabla P_{n+1} - \rho_w \mathbf{g}\right)\cdot\nabla\xi \\
&- \sum_{e\in\Gamma_h^i}\int_e (\lambda_w(S_{n+1}))^{\uparrow \mathbf{v}_w^n}\{K\left(\nabla P_{n+1} - \rho_w \mathbf{g}\right)\cdot\mathbf{n}_e\}[\xi] - \sum_{e\in\Gamma^{\mathrm{D},s}}\int_e \lambda_w(g^s)K\left(\nabla P_{n+1} - \rho_w \mathbf{g}\right)\cdot\mathbf{n}\,\xi \\
&- \sum_{e\in\Gamma^{\mathrm{out}}}\int_e \lambda_w(S_{n+1})K\left(\nabla P_{n+1} - \rho_w \mathbf{g}\right)\cdot\mathbf{n}_e\,\xi + \sum_{e\in\Gamma_h^i\cup\Gamma^{\mathrm{D},s}}\frac{\sigma}{h}\int_e [S_{n+1}][\xi] \\
&= \int_\Omega q_w(S_n)\xi + \frac{1}{\tau}\int_\Omega \phi S_n\xi + \frac{\sigma}{h}\int_{\Gamma^{\mathrm{D},s}} g^s\xi + \int_{\Gamma^{\mathrm{N},s}} j^s\xi, \qquad \forall\xi\in\mathcal{D}(\mathcal{E}_h).
\end{aligned} \tag{3.4}$$

The penalty parameter σ is constant on the interior edges and its value is chosen 10 times larger on the Dirichlet boundaries. The quantities $(\cdot)^{\uparrow \mathbf{v}_\ell^n}$ and $(\cdot)^{\uparrow \mathbf{v}_w^n}$ denote the upwind values with respect to the vector functions $\mathbf{v}_\ell^n$ and $\mathbf{v}_w^n$ that are scaled quantities of the phase velocities. They depend on the pressure and saturation evaluated at the previous time t_n:

$$\mathbf{v}_w^n = -K\left(\nabla P_n - \rho_w \mathbf{g}\right), \quad \mathbf{v}_\ell^n = -K\left(\nabla P_n + \nabla P_c(S_n) - \rho_\ell \mathbf{g}\right)$$

The definition of the upwind operator with respect to a generic discontinuous vector field $\mathbf{v}$ is:

$$\forall e = \partial E^+ \cap \partial E^-, \quad \xi^{\uparrow \mathbf{v}}|_e = \begin{cases} \xi|_{E^+}, & \text{if} \quad \{\mathbf{v}\}\cdot\mathbf{n}_e > 0, \\ \xi|_{E^-}, & \text{if} \quad \{\mathbf{v}\}\cdot\mathbf{n}_e \leq 0. \end{cases}$$

At the initial time, the discrete saturation is the L^2 projection of the initial condition.

$$\int_\Omega S_0 v = \int_\Omega s_0 v, \quad \forall v \in \mathcal{D}(\mathcal{E}_h).$$

At each time step, we solve (3.3)–(3.4) together with a Newton solver, followed by flux and slope limiters (see Algorithm 1). Fig. 1 is a schematic that describes the actions of both flux and slope limiters on the discrete saturation. The convergence analysis of the proposed scheme remains an open problem. The reader might be interested in the error analysis of a DG scheme for a different formulation of two-phase flow in [36] and also in the convergence analysis of finite volume methods and finite element methods for the PDEs (2.1)–(2.3) in [37–39]. The next two sections describe these limiters in detail and contain a proof that the resulting saturation is bound-preserving.

Algorithm 1 DG+FL+SL method

Compute initial saturation S_0
for $n = 0, \ldots, (N_\tau - 1)$ **do**
  Solve (3.3)–(3.4) with Newton's method
  Apply flux limiter: $S_{n+1}^{\mathrm{FL}} = \mathcal{L}_{\mathrm{flux}}(S_{n+1})$
  Apply slope limiter to $S_{n+1} = \mathcal{L}_{\mathrm{slope}}(S_{n+1}^{\mathrm{FL}})$
end for

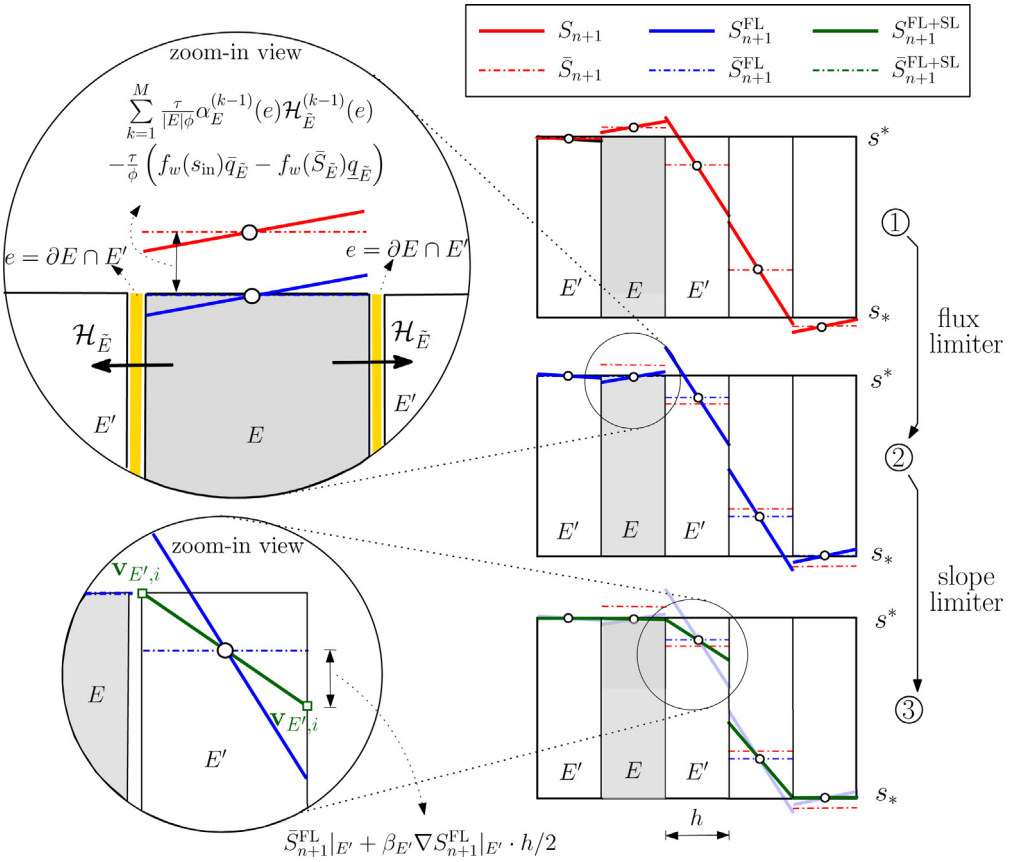

Fig. 1. Schematic of flux and slope limiters to achieve a pointwise bound-preserving DG solution: Unlimited DG solution (figure ①) is found to violate the upper bound s^* and lower bound s_*. After implementing the flux limiter in a post-processing step, the local average values shown in broken blue lines are bounded (figure ②). The non-physical fluxes are limited by using the limiting factor $\alpha_E^{(k-1)}(e) \in [0, 1]$ at the discrete level and performing multiple correction cycles (see Section 3.1). Note that this procedure is mass conservative and we observe that the decrease of the average value on element E brings about an increase on the average value of neighboring elements E'. We subsequently apply a slope limiting procedure to produce pointwise bound-preserving solutions (see Section 3.2). The correction factor $\beta_E \in [0, 1]$ at each element vertex $\mathbf{v}_{E,i}$ takes the average values of neighboring elements as local bounds and determines the maximum admissible slope (figure ③). Note that the local average values are left unchanged during the slope limiting. (For interpretation of the references to color in this figure legend, the reader is referred to the web version of this article.)

3.1. Flux limiter

The flux limiter will enforce that the element-wise average of the saturation satisfies the desired physical bounds. The idea of limiting the fluxes by an iterative procedure was introduced by Zalesak in [40] and was further investigated by Kuzmin and Gorb [28]. The novelty of our flux limiter is in the handling of the source and sink terms, as well as a different way to update the element-wise average. We assume that the saturation at the previous

time step, t_n, satisfies:

$$s_* \le S_n(\mathbf{x}) \le s^*, \quad \forall \mathbf{x} \in \Omega. \tag{3.5}$$

for some constants $0 \le s_* \le s^* \le 1$. The flux limiting is applied to each element E given the element-wise average of the saturation at the previous and current time steps and given a flux function defined on each face $e \subset \partial E$. First we compute the element-wise average at time t_n and t_{n+1}:

$$\overline{S_i}|_E = \overline{S_{i,E}}, \quad \overline{S_{i,E}} = \frac{1}{|E|}\int_E S_i, \quad \forall E \in \mathcal{E}_h, \quad i = n, n+1.$$

Next, for a fixed element E, let $\mathbf{n}_E$ be the unit outward normal vector to E. We define the flux function $\mathcal{H}_{n+1}|_E = \mathcal{H}_{n+1,E}$ as follows:

$$\begin{aligned} \forall e = \partial E \cap \partial E', \quad \mathcal{H}_{n+1,E}(e) = &-\int_e (\lambda_w(S_{n+1}))^{\uparrow \mathbf{v}_w^n}\{K\big(\nabla P_{n+1} - \rho_w \mathbf{g}\big)\cdot \mathbf{n}_E\} \\ &+ \frac{\sigma}{h}\int_e (S_{n+1}|_E - S_{n+1}|_{E'}) \end{aligned} \tag{3.6}$$

$$\forall e \in \partial E \cap \Gamma^{\mathrm{D},s}, \quad \mathcal{H}_{n+1,E}(e) = -\int_e \lambda_w(g^s)K\big(\nabla P_{n+1} - \rho_w \mathbf{g}\big)\cdot \mathbf{n}_E + \frac{\sigma}{h}\int_e (S_{n+1} - g^s), \tag{3.7}$$

$$\forall e \in \partial E \cap \Gamma^{\mathrm{N},s}, \quad \mathcal{H}_{n+1,E}(e) = \int_e j^s, \tag{3.8}$$

$$\forall e \in \partial E \cap \Gamma^{\mathrm{out}}, \quad \mathcal{H}_{n+1,E}(e) = \int_e \lambda_w(S_{n+1})K(\nabla P_{n+1} - \rho_w \mathbf{g})\cdot \mathbf{n}_E. \tag{3.9}$$

For an interior face e of the element E, the quantity $\mathcal{H}_{n+1,E}(e)$ measures the net mass flux across e into the neighboring element E' that also shares the face e. We note that:

$$\mathcal{H}_{n+1,E}(e) = -\mathcal{H}_{n+1,E'}(e).$$

After application of the flux limiter operator, the limited saturation has a possibly different cell-average:

$$S_{n+1}^{\mathrm{FL}} = \mathcal{L}_{\mathrm{flux}}(S_{n+1}), \quad S_{n+1}^{\mathrm{FL}}(\mathbf{x}) = S_{n+1}(\mathbf{x}) - \overline{S_{n+1,E}} + \bar{S}_{n+1}^{\mathrm{FL}}|_E, \quad \forall \mathbf{x} \in E. \tag{3.10}$$

The new cell-average of the saturation is obtained by an iterative process, that takes for input the cell average at the previous time step and the flux function:

$$\bar{S}_{n+1}^{\mathrm{FL}} = \mathcal{L}_{\mathrm{avg}}(\overline{S_n}, \mathcal{H}_{n+1}).$$

Before showing that the limited saturation satisfies (3.5), we describe the algorithm for the operator $\mathcal{L}_{\mathrm{avg}}$.

3.1.1. The algorithm for $\mathcal{L}_{\mathrm{avg}}$

For a fixed element E, we denote by $\mathcal{N}_E$ the set of elements that include E and all neighboring elements E' that share a face e with E. The algorithm constructs a sequence of flux functions and element-wise averages for E and its neighbors E'. While the construction of the element-wise averages are local to E and its neighbors E', the stopping criterion is global to ensure bound-preserving solutions. We first initialize the sequences with the input arguments:

$$\bar{S}_{\tilde{E}}^{(0)} = \overline{S_{n,\tilde{E}}}, \quad \mathcal{H}_{\tilde{E}}^{(0)}(e) = \mathcal{H}_{n+1,\tilde{E}}(e), \quad \forall e \in \partial \tilde{E}, \quad \forall \tilde{E} \in \mathcal{N}_E.$$

Next, for $k \ge 1$, we have the following steps:

Step 1 Compute inflow and outflow fluxes:

$$P_{\tilde{E}}^{+} = \tau \sum_{e \in \partial \tilde{E}} \max(0, -\mathcal{H}_{\tilde{E}}^{(k-1)}(e)), \quad P_{\tilde{E}}^{-} = \tau \sum_{e \in \partial \tilde{E}} \min(0, -\mathcal{H}_{\tilde{E}}^{(k-1)}(e)), \quad \forall \tilde{E} \in \mathcal{N}_E. \tag{3.11}$$

Step 2 Compute admissible upper and lower bounds for all $\tilde{E} \in \mathcal{N}_E$:

$$Q_{\tilde{E}}^{+} = |\tilde{E}|\Big(\phi s^* - \phi \bar{S}_{\tilde{E}}^{(k-1)} - \gamma_{1k}\tau\big(f_w(s_{\mathrm{in}})\bar{q}_{\tilde{E}} - f_w(\bar{S}_{\tilde{E}}^{(k-1)})\underline{q}_{\tilde{E}}\big)\Big), \tag{3.12}$$

$$Q_{\tilde{E}}^{-} = |\tilde{E}|\Big(\phi s_* - \phi \bar{S}_{\tilde{E}}^{(k-1)} - \gamma_{1k}\tau\big(f_w(s_{\text{in}})\bar{q}_{\tilde{E}} - f_w(\bar{S}_{\tilde{E}}^{(k-1)})\underline{q}_{\tilde{E}}\big).\Big) \tag{3.13}$$

The scalar factor γ_{1k} is equal to 1 if $k = 1$ and 0 otherwise. The injection and production well rates, restricted to any element $\tilde{E}$, are denoted by $\bar{q}_{\tilde{E}}$ and $\underline{q}_{\tilde{E}}$ respectively. They are assumed to be piecewise constant fields; otherwise we take the element-wise average of the flow rates.

Step 3 Compute limiting factors $\alpha_E^{(k-1)}(e)$ for all faces $e \subset \partial E$. If e is an interior face such that $e = \partial E \cap \partial E'$:

$$\alpha_E^{(k-1)}(e) = \begin{cases} \min\big(\min(1, Q_E^+/P_E^+), \min(1, Q_{E'}^-/P_{E'}^-)\big) & \text{if} \quad \mathcal{H}_E^{(k-1)}(e) < 0, \\ \min\big(\min(1, Q_E^-/P_E^-), \min(1, Q_{E'}^+/P_{E'}^+)\big) & \text{if} \quad \mathcal{H}_E^{(k-1)}(e) > 0. \end{cases}$$

If e is a boundary face:

$$\alpha_E^{(k-1)}(e) = \begin{cases} \min(1, Q_E^+/P_E^+) & \text{if} \quad \mathcal{H}_E^{(k-1)}(e) < 0, \\ \min(1, Q_E^-/P_E^-) & \text{if} \quad \mathcal{H}_E^{(k-1)}(e) > 0. \end{cases}$$

Step 4 Update $\bar{S}_E^{(k)}$ and $\mathcal{H}_E^{(k)}(e)$ as follows:

$$\bar{S}_E^{(k)} = \bar{S}_E^{(k-1)} - \frac{\tau}{\phi|E|}\sum_{e\subset\partial E}\alpha_E^{(k-1)}(e)\mathcal{H}_E^{(k-1)}(e) + \frac{\gamma_{1k}\,\tau}{\phi}\Big(f_w(s_{\text{in}})\bar{q}_E - f_w(\bar{S}_E^{(k-1)})\underline{q}_E\Big), \tag{3.14}$$

$$\mathcal{H}_E^{(k)}(e) = (1 - \alpha_E^{(k-1)}(e))\,\mathcal{H}_E^{(k-1)}(e), \quad \forall e \subset \partial E. \tag{3.15}$$

Step 5 Define a global stopping criterion
If $\Big(\max_{E\in\mathcal{E}_h}\max_{e\in\partial E}|\mathcal{H}_E^{(k)}(e)| < \epsilon_1\Big)$ or $\Big(\max_{E\in\mathcal{E}_h}\max_{e\in\partial E}|\mathcal{H}_E^{(k)}(e) - \mathcal{H}_E^{(k-1)}(e)| < \epsilon_2\Big)$
return $\bar{S}_{n+1}^{\text{FL}}|_E = \bar{S}_E^{(k)}$.
Else
set $k \leftarrow k+1$ and go to Step 1.

3.1.2. Bound-preserving solutions

In this section, we show that the solution S_{n+1}^{FL} obtained in (3.10) has a cell-average that is bound-preserving for the case where flow is driven by boundary conditions only (no wells). Clearly, it suffices to show that $\bar{S}_{n+1}^{\text{FL}}$ is bound-preserving. This is done in two steps. First, we show that each iterate in the flux-limiter algorithm is bound preserving. Second, we show that the stopping criterion is reached for some value k_0.

Lemma 3.1. *Let E be a mesh element and let $(\bar{S}_E^{(k)})_k$ be the sequence obtained in the algorithm $\mathcal{L}_{\text{flux}}$. Assume that the iterate $\bar{S}_E^{(k-1)}$ belongs to the interval $[s_*, s^*]$. Then the next iterate $\bar{S}_E^{(k)}$ also belongs to the interval $[s_*, s^*]$.*

Proof. Let us check the upper bound: $\bar{S}_E^{(k)} \le s^*$. Since for an interior face e, we have: $\alpha_E^{(k-1)}(e) = \alpha_{E'}^{(k-1)}(e)$, it is easy to check by induction on k that $\mathcal{H}_E^{(k)}(e) = -\mathcal{H}_{E'}^{(k)}(e)$. Since the iterate $\bar{S}_E^{(k-1)}$ belongs to the interval $[s_*, s^*]$, it then follows by its definition that $\alpha_E^{(k-1)}(e) \ge 0$ for all $e \subset \partial E$. We then apply the inequality $x \le \max(0, x)$ to (3.14) to obtain:

$$\begin{aligned} \bar{S}_E^{(k)} \le& \bar{S}_E^{(k-1)} + \frac{\tau}{\phi|E|}\sum_{e\subset\partial E}\alpha_E^{(k-1)}(e)\max(0, -\mathcal{H}_E^{(k-1)}(e)) \\ \le& \bar{S}_E^{(k-1)} + \frac{\tau}{\phi|E|}\sum_{e\subset\partial E}\frac{Q_E^+}{P_E^+}\max(0, -\mathcal{H}_E^{(k-1)}(e)) \\ \le& \bar{S}_E^{(k-1)} + \frac{1}{\phi|E|}Q_E^+. \end{aligned} \tag{3.16}$$

Therefore with the definition of Q_E^+ we have

$$\bar{S}_E^{(k)} \le \bar{S}_E^{(k-1)} + (s^* - \bar{S}_E^{(k-1)}) = s^*.$$

The proof for the lower bound $\bar{S}_E^{(k)} \ge S_*$ follows a similar argument, after applying the identity $x \ge \min(0, x)$ to (3.14). □

Lemma 3.2. *Assume that the cell averages $\overline{S_{n,E}}$ at time t_n belong to the interval $[s_*, s^*]$ for all elements E. Then we have*

$$s_* \le \bar{S}^{\mathrm{FL}}_{n+1}|_E \le s^*, \quad \forall E \in \mathcal{E}_h.$$

Proof. With Lemma 3.1, it suffices to show that the sequence $(\mathcal{H}^{(k)}_E(e))$ converges as k tends to infinity, for all E in $\mathcal{E}_h$ and for all $e \in \partial E$. With (3.15), and since $\alpha^{(k-1)}_E$ belongs to [0, 1], it is easy to show by induction on k that

$$\max_{E\in\mathcal{E}_h}\max_{e\subset\partial E}|\mathcal{H}^{(k)}_E(e)| \le \max_{E\in\mathcal{E}_h}\max_{e\subset\partial E}|\mathcal{H}^{(k-1)}_E(e)|.$$

This implies convergence of $(\mathcal{H}^{(k)}_E(e))$ for all elements E, so that there exists k_0 such that

$$\left(\max_{E\in\mathcal{E}_h}\max_{e\in\partial E}|\mathcal{H}^{(k_0)}_E(e)| < \epsilon_1\right), \text{ or } \left(\max_{E\in\mathcal{E}_h}\max_{e\in\partial E}|\mathcal{H}^{(k_0)}_E(e) - \mathcal{H}^{(k_0-1)}_E(e)| < \epsilon_2\right).$$

Since $\bar{S}^{\mathrm{FL}}_{n+1}|_E = \bar{S}^{k_0}_E$, we conclude the proof. □

3.2. Slope limiter

The slope limiter operator, denoted by $\mathcal{L}_{\mathrm{slope}}$, is applied to the discrete saturation S^{FL}_{n+1} at each time step. The element-wise mean values of the saturation are left unchanged by this procedure. There is a variety of slope limiters available in the literature. For convenience, we choose a vertex-based slope limiter that is well suited for piecewise linear polynomials [25] and that consists of two steps.

(i) We first mark the elements in which the maximum principle is not satisfied (i.e., $S^{\mathrm{FL}}_{n+1}(\mathbf{x}) > s^*$ or $S^{\mathrm{FL}}_{n+1}(\mathbf{x}) < s_*$). We will apply the slope limiter on these marked elements only.

(ii) By a Taylor expansion around the centroid $\mathbf{c}_E$ of element E, the linear saturation takes the form

$$S^{\mathrm{FL}}_{n+1}|_E(\mathbf{x}) = \bar{S}^{\mathrm{FL}}_{n+1,E} + \nabla S^{\mathrm{FL}}_{n+1}\cdot(\mathbf{x}-\mathbf{c}_E), \quad \forall \mathbf{x}\in E. \tag{3.17}$$

For the marked elements, a slope limiter replaces the local solution $S^{\mathrm{FL}}_{n+1}|_E$ by the following linear constrained reconstruction

$$S_{n+1}(\mathbf{x}) = \bar{S}^{\mathrm{FL}}_{n+1,E} + \beta_E\nabla S^{\mathrm{FL}}_{n+1}\cdot(\mathbf{x}-\mathbf{c}_E), \quad \forall \mathbf{x}\in E. \tag{3.18}$$

Let $\mathbf{v}_{E,i}$ denote the ith vertex of element E. We determine the maximum admissible slope for the constrained reconstruction by choosing values $\beta_E \in [0, 1]$ such that boundedness of S_{n+1} is satisfied at all vertices of E:

$$S^{E,i}_* \le S_{n+1}(\mathbf{v}_{E,i}) \le S^*_{E,i}, \tag{3.19}$$

where $S^{E,i}_*$ and $S^*_{E,i}$ are defined as maximum and minimum means values of the saturation over all the elements (including E) that contain the vertex $\mathbf{v}_{E,i} \in E$.

$$S^{E,i}_* = \min_{E'\in\mathcal{E}_h|\mathbf{v}_{E,i}\in E'} \bar{S}^{\mathrm{FL}}_{n+1,E'}, \quad S^*_{E,i} = \max_{E'\in\mathcal{E}_h|\mathbf{v}_{E,i}\in E'} \bar{S}^{\mathrm{FL}}_{n+1,E'}. \tag{3.20}$$

The bounds of the saturation at all vertices are guaranteed if the correction factor β_E is chosen as:

$$\beta_E = \min_i \begin{cases} \frac{S^*_{E,i}-\bar{S}^{\mathrm{FL}}_{n+1,E}}{S^{\mathrm{FL}}_{n+1}(\mathbf{v}_{E,i})-\bar{S}^{\mathrm{FL}}_{n+1,E}} & \text{if} \quad S^{\mathrm{FL}}_{n+1}(\mathbf{v}_{E,i}) > S^*_{E,i}, \\ 1 & \text{if} \quad S^{E,i}_* \le S^{\mathrm{FL}}_{n+1}(\mathbf{v}_{E,i}) \le S^*_{E,i}, \\ \frac{S^{E,i}_*-\bar{S}^{\mathrm{FL}}_{n+1,E}}{S^{\mathrm{FL}}_{n+1}(\mathbf{v}_{E,i})-\bar{S}^{\mathrm{FL}}_{n+1,E}} & \text{if} \quad S^{\mathrm{FL}}_{n+1}(\mathbf{v}_{E,i}) < S^{E,i}_*. \end{cases} \tag{3.21}$$

Using all the previous results, we obtain that the discrete saturation is bound-preserving.

Proposition 3.1. *Let $(S_{n+1})_n$ be the sequence of discrete saturations defined by Algorithm 1. Assume that the initial saturation is bounded below and above by s_* and s^* respectively. Then, we have*

$$s_* \le S_{n+1}(\mathbf{x}) \le s^*, \quad \forall \mathbf{x}\in\Omega. \tag{3.22}$$

3.3. Computer implementation and solvers

We implement the proposed computational framework using the finite element capabilities in Firedrake Project [41–45] with GNU compilers. Firedrake is built upon several scientific packages and can employ various computing tools across either CPUs or GPUs. Software dependencies can be accessed at [46–52]. The structured meshes are generated internally on top of DMPlex grid format [53] and unstructured meshes are imported from GMSH [54].

We utilize the MPI-based PETSc library [55–57] as the linear algebra back-end to solve nonlinear equations (3.3)–(3.4). We use Newton's method with (damped) step line search technique [58] and set the relative convergence tolerance to 10^{-6}. For the inner linear solve at each Newton iteration, we rely on the MUMPS direct solver [59,60] with relative pivoting threshold of 0.01. MUMPS uses several efficient preordering algorithms to permute the columns of matrix and thereby minimize the fill-in (number of nonzeros in the factorization) in the LU factorization. At each time step, following the Newton solver convergence, we apply flux and slope limiters. Implementation of the flux limiter algorithm discussed in Section 3.1 is provided in the module FluxLimiter along with an auxiliary flux wrapper module named Hsign. Global stopping criteria for all problem sets are taken as $\epsilon_1 = \epsilon_2 = 10^{-6}$. As for the slope limiter, we use the native VertexBasedLimiter module embedded in the Firedrake project. All simulations are conducted on a single socket Intel i5-8257U node by utilizing a single MPI process.

Codes used to perform experiments in this paper are publicly available at msarrafj/LimitedDG [61] repository. Firedrake and its component may be obtained from https://www.firedrakeproject.org/. For reproducibility, we also cite archives of the exact software versions used to produce results in this paper. All major Firedrake components have been archived on Zenodo/firedrake [62]. This record collates DOIs for the components and can be installed following the instructions at https://www.firedrakeproject.org/download.html.

4. Numerical results

In this section, several numerical experiments are carried out in following order: (i) We first validate our proposed method on two benchmark problems: one-dimensional Buckley–Leverett problem and two-dimensional Buckley–Leverett problem with gravity. Further, we investigate the convergence rates by using method of manufactured solutions and verify that the flux limiter preserves accuracy. (ii) We then perform various pressure-driven flow problems on structured and unstructured meshes, to study the efficacy of limiters on capturing high-accuracy wetting phase saturation profiles. (iii) The robustness of the scheme in the presence of injection and production wells is assessed using the quarter five-spot problem, with homogeneous and discontinuous highly varying permeability fields. For both pressure-driven flow problem and quarter five-spot problems, we examine the element-wise mass balance property associated with the limiters and highlight the capability of the saturation in satisfying the maximum-principle. (iv) Finally, we study the influence of gravity on the flows by testing our scheme with three different gravity numbers.

For all problems, we assume the following parameters unless otherwise specified:

$$\rho_w = 1000 \text{ kg/m}^3, \quad \rho_\ell = 850 \text{ kg/m}^3,$$
$$\phi = 0.2, \quad s_{rw} = 0.2, \quad s_{r\ell} = 0.15, \quad s_0 = 0.2, \quad P_0 = 10^6 \text{ Pa}.$$

The residual saturations imply the physical lower and upper bounds for the saturation:

$$s_* = s_{rw} = 0.2, \quad s^* = 1 - s_{r\ell} = 0.85.$$

4.1. Verification

4.1.1. One-dimensional Buckley–Leverett problem

The original Buckley–Leverett transport equation introduced in 1942 [63], also known as the frontal-advance equation, is a well-known non-linear hyperbolic equation for the description of one-dimensional immiscible displacement in a linear reservoir. Because the problem has a semi-analytical solution, it is widely used to validate numerical methods for two-phase flows in porous media. Since capillary pressure and gravity are neglected, the total velocity of the phases $\mathbf{u}_t = (u_t, v_t)^T$ can be written as:

$$\mathbf{u}_t = -(\lambda_w + \lambda_\ell) K \nabla P. \tag{4.1}$$

By substituting ∇P from (4.1) into Eq. (2.6) and ignoring source/sink terms, we obtain the general form of the Buckley–Leverett equation.

$$\frac{\partial}{\partial t}(\phi S) - \nabla \cdot \mathbf{f}_{BL} = 0, \quad \text{in} \quad \Omega \times (0, T). \tag{4.2}$$

The convection flux $\mathbf{f}_{BL} = (F(S), G(S))^T$ reduces in one-dimension to:

$$F(S) = \frac{\lambda_w(S) u_t}{\lambda_w(S) + \lambda_\ell(S)}, \text{ and } \quad G(S) = 0. \tag{4.3}$$

The relative permeabilities are chosen as:

$$k_{rw}(S) = S^4, \ k_{r\ell}(S) = (1 - S)^2(1 - S^2). \tag{4.4}$$

We take an interval domain $\Omega = [0, 300]$ m with uniform mesh, and we fix the following parameters:

$$u_t = 3 \times 10^{-7}\text{m/s}, \ \mu_w = \mu_\ell = 1\text{Pa s}, \ s_0 = 0.1, \ h = 12\text{m}, \ \tau = 22.2\text{days}.$$

The Dirichlet boundary condition of $g^s = 0.85$ is weakly prescribed at the left boundary $x = 0$. We assume outflow boundary at $x = 300$. This setup gives rise to the classical Buckley–Leverett profile, which consists of a shock wave immediately followed by a rarefaction wave. It should be noted that neither higher order nor lower order DG approximation of saturation (without bound-preserving mechanism) can completely suppress violations with respect to maximum principle [64–66]. Here, we employ the first-order implicit DG formulation with our proposed limiter scheme to discretize Eqs. (4.2)–(4.3) in space, and backward Euler scheme is utilized in time. The DG penalty parameter is set to $\sigma = 10^{-6}$ and the flux $\mathbf{f}_{BL}$ is approximated with a first-order upwind method [66,67] as it provides good results in conjunction with proposed limiters. To implement the flux limiter, the following flux functional $\mathcal{H}_E(e)$ is adopted on each face $e \subset \partial E$:

$$\forall e = \partial E \cap \partial E', \ \mathcal{H}_{n+1,E}(e) = \int_e \{\mathbf{f}_{BL}(S_{n+1})\} \cdot \mathbf{n}_E + \frac{1}{2} \int_e \left| \frac{d\mathbf{f}_{BL}(S_n)}{dS} \cdot \mathbf{n}_E \right| \left(S_{n+1}|_E - S_{n+1}|_{E'} \right),$$

$$\forall e \in \partial E \cap \Gamma^{\mathrm{D},s}, \ \mathcal{H}_{n+1,E}(e) = \int_e \mathbf{f}_{BL}(g^s) \cdot \mathbf{n}_E,$$

$$\forall e \in \partial E \cap \Gamma^{\mathrm{out},s}, \ \mathcal{H}_{n+1,E}(e) = \int_e \mathbf{f}_{BL}(S_{n+1}) \cdot \mathbf{n}_E.$$

The final simulation time is $T = 800$ days, and the saturation profile is depicted in Fig. 2 for $t = 400$ and $t = 800$ days. We performed a four-step mesh refinement study and linearly refined τ at each step. We observe that the location of the front obtained from the proposed numerical scheme is in good agreement with the location of the front for the analytical solution even for the case of coarse mesh and as we proceed with refinement, the discrete solution converges to the analytical solution. To calculate the semi-analytical solution of Buckley–Leverett equation (i.e., the position of the saturation front), we resorted to Welge graphical method [68]. Fig. 2 also provides a zoom-in view at the location of front for $t = 800$ days for better visualization. As expected, the numerical saturation remains within physical bounds and no undershoots and overshoots are observed. The choice of implicit time marching algorithm is shown to have no erroneous smearing effect on the saturation front.

4.1.2. Buckley–Leverett problem with gravity

In this numerical experiment, we study the effect of proposed limiters in the two-dimensional Buckley–Leverett equation that incorporates gravitational effects along the y-axis [69–71]. Consider equation (4.2) with the following non-convex flux functions in the x- and y- directions:

$$F(S) = \frac{\lambda_w(S) u_t}{(\lambda_w(S) + \lambda_\ell(S))}, \quad G(S) = \frac{F(S) v_t}{u_t}(1 - 5\lambda_\ell). \tag{4.5}$$

This benchmark problem was solved by finite element method combined with operator-splitting method in [72]. For comparison purpose, hence, we take $u_t = v_t = 1$ m/s, $\lambda_w(S) = S^2$, $\lambda_\ell(S) = (1 - S^2)$ and $\phi = 1$. We solve (4.2) and (4.5) on the square domain $[0, 3]^2$ m^2 with structured triangular mesh of size $h = 0.03$ m subject to the initial condition:

$$s_0(x, y) = \begin{cases} 1, & \text{for } (x - 1.5)^2 + (y - 1.5)^2 < 0.5 \\ 0, & \text{otherwise.} \end{cases} \tag{4.6}$$

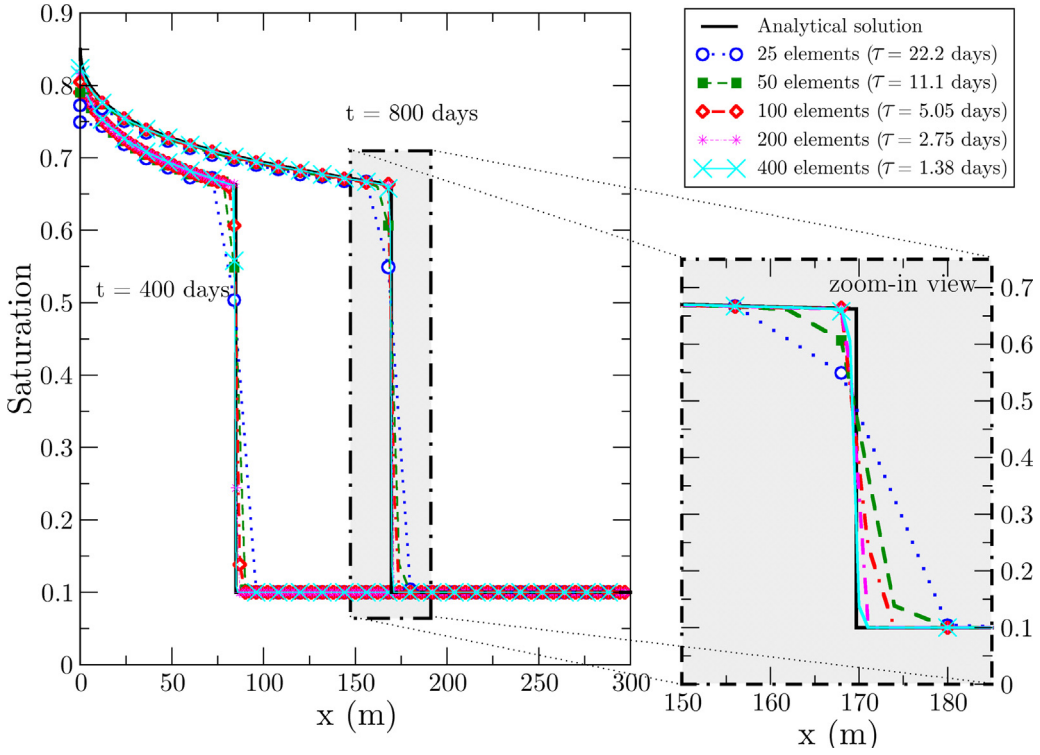

Fig. 2. One-dimensional Buckley–Leverett problem: This figure shows the saturation profiles obtained from the limited DG scheme at two different time-steps $t = 400$ days and $t = 800$ days. As we refine the mesh, the approximation converges to the analytical solution. The numerical solution is satisfactory with respect to maximum principle as no undershoots and overshoots are observed.

Finally, we impose no flow condition $\mathbf{u_t} \cdot \mathbf{n} = 0$ everywhere on the boundary $\partial\Omega$. Similar to the one-dimensional problem, we use backward Euler time marching and discretize the problem with implicit DG formulation (with $\sigma = 0.1$) augmented with the proposed flux and slope limiters scheme. Herein, the flux limiter functional $\mathcal{H}_{n+1,E}(e)$ on the interior edges is the same as that of the one-dimensional Buckley–Leverett and on all exterior edges it is set to 0. The simulation runs to $T = 0.5$ s with 440 time steps. In Fig. 3, we show the numerical results at the final time obtained from the implicit DG formulation without limiters (see Fig. 3(a)) and with limiters (see Fig. 3(b)). We compare the results with the reference solution. Evidently, DG scheme with no limiters produces an oscillatory solution that results in strong violations with respect to maximum principle. However, the application of limiters gives rise to bound-preserving solution (i.e., $0 \leq S_{n+1} \leq 1$); and undershoots and overshoots are eliminated completely. This result does not exhibit extra numerical diffusion and is consistent with the reference solution shown in Fig. 3(c).

4.1.3. Convergence study

In order to verify convergence properties of our limiter scheme, we perform h-convergence study on a problem constructed by the method of manufactured solutions and on a Buckley–Leverett problem discussed on Section 4.1.1. For both problems the convergence properties are computed by using a time step $\tau = O(h^2)$. First, we carry out the study on two-dimensional structured triangular meshes. The computational domain Ω is the unit square and the exact solutions are:

$$s(x, y, t) = 0.4 + 0.4xy + 0.2\cos(t + x), \tag{4.7a}$$

$$p(x, y, t) = 2 + x^2 y - y^2 + x^2 \sin(y + t) - \frac{1}{3}\cos(t) + \frac{1}{3}\cos(t + 1) - \frac{11}{6}. \tag{4.7b}$$

Through the method of manufactured solutions, we replace the source/sink terms (i. e., wells flow rates) of Eqs. (2.5)–(2.6) by body force terms obtained from manufactured solutions. Dirichlet boundary conditions are

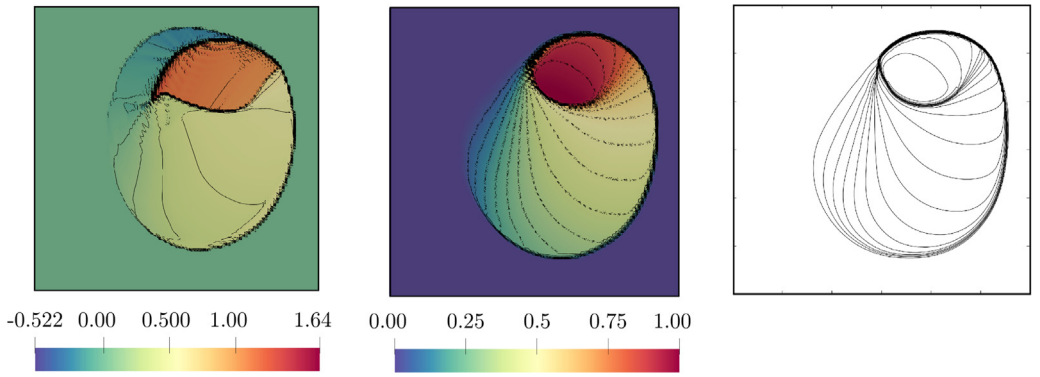

(a) DG approximation (b) DG approximation with flux and slope limiters (c) Finite element with corrected operator splitting [Karlsen et al., 1998]

Fig. 3. Two-dimensional Buckley–Leverett problem with gravity subject to the initial condition (4.6): This figure shows saturation approximations and contour plots at $t = 0.5$ s. Solutions are obtained using the DG scheme without limiter (left) and with the proposed the flux and slope limiters (middle); and are compared with a benchmark solution on fine mesh (right). DG method without any bound-preserving mechanism fails to predict the correct profile and non-physical values are generated (i.e., $S_{n+1} \in [-0.52, +1.64]$). However, the DG solution post-processed with limiters is accurate and satisfies the maximum-principle.

applied on $\partial\Omega$ on both saturation and pressure fields. The input parameters are:

$$\phi = 0.2,\ K = 1\,\mathrm{m}^2,\ \mu_w = \mu_\ell = 1\,\mathrm{Pa\,s},\ s_{rw} = s_{r\ell} = 0,\ k_{rw}(S) = S^2,\ k_{r\ell}(S) = (1-S)^2.$$

The capillary pressure is based on Brooks–Corey model:

$$P_c(S) = \begin{cases} p_d S^{\frac{-1}{\theta}} & \text{if } S > R \\ p_d R^{\frac{-1}{\theta}} - \frac{p_d}{\theta} R^{-1-\frac{1}{\theta}}(S-R) & \text{otherwise,} \end{cases} \tag{4.8}$$

where the entry pressure is set to $p_d = 50$ Pa, inhomogeneity characterization parameter is set to $\theta = 2$, and linearization tolerance is set to $R = 0.05$. This regularization of the capillary pressure is commonly used in numerical simulations of two-phase flows and it yields a bounded derivative of the capillary pressure [17]. We note that the admissible global bounds for the flux limiter algorithm are updated throughout the simulation. In other words, at every time step, s_* and s^* bounds are determined by the maximum and minimum of the exact solution (4.7a), respectively. When using the limiters no upper and lower bound violations are observed in the discrete solution. Table 1 shows the errors in L^2 and H^1 norms evaluated at $T = 1$ s and the corresponding convergence rates for saturation and pressure. Similarly, the h-convergence results for the one-dimensional Buckley–Leverett problem at $t = 800$ days are presented in Table 2. We compare rates for four cases: (i) no limiters (DG), (ii) with both flux and slope limiters (DG+FL+SL), (iii) with only slope limiter (DG+SL), and (iv) with only flux limiter (DG+FL). For both problems, DG returns expected optimal convergence rates of 2 in the L^2 norm and 1 in the H^1 norm. However, we observe that applying both limiters results in suboptimal rates. Cases (iii) and (iv) indicate that the application of flux limiters only preserves optimal rates whereas the application of slope limiters only yields a decline in the convergence rates. The slope limiter scheme taken from [25] is completely independent of the proposed flux limiter in Section 3. Designing a slope limiter that produces optimal rates remains a challenge.

We show in Tables 3 and 4 the errors in the L^2 norm of the cell average for the saturation and the corresponding convergence rates. For both problems optimal rate of 2 is obtained for either DG or DG+FL+SL. This result reiterates that the flux limiter does not reduce the accuracy and the slope limiter does not impact the rates since it does not alter the element-wise averages.

4.2. Two-dimensional pressure-driven flow

We take a computational domain of $\Omega = [0, 100]^2$ m^2 with zero gravity field for all problems in this section. The wetting phase is injected along the left boundary and the non-wetting phase is pushed out through the right

Table 1
Problem constructed by the method of manufactured solutions: errors in L^2 and H^1 norms and convergence rates, for $\tau = h^2$ and $T = 1$ s. Note that flux limiter algorithm preserves the accuracy of the DG discretization. However, slope limiter slightly degrades the rates of convergence.

	h	$\|\|S_n - S(T)\|\|_{L^2(\Omega)}$	Rate	$\|\|P_n - P(T)\|\|_{L^2(\Omega)}$	Rate	$\|\|S_n - S(T)\|\|_{H^1(\Omega)}$	Rate	$\|\|P_n - P(T)\|\|_{H^1(\Omega)}$	Rate
i. DG	1/2	9.454×10^{-4}	–	7.607×10^{-3}	–	7.480×10^{-3}	–	7.325×10^{-2}	–
	1/4	5.373×10^{-4}	0.82	2.999×10^{-3}	1.34	4.319×10^{-3}	0.79	4.248×10^{-2}	0.79
	1/8	1.732×10^{-4}	1.63	8.690×10^{-4}	1.79	1.836×10^{-3}	1.23	2.322×10^{-2}	0.87
	1/16	4.633×10^{-5}	1.90	2.303×10^{-4}	1.92	8.374×10^{-4}	1.13	1.245×10^{-2}	0.90
	1/32	1.176×10^{-5}	1.98	5.912×10^{-5}	1.96	4.103×10^{-4}	1.03	6.492×10^{-3}	0.94
ii. DG+FL+SL	1/2	$1.720 \times 10^{+0}$	–	3.180×10^{-2}	–	$1.740 \times 10^{+0}$	–	2.110×10^{-1}	–
	1/4	7.620×10^{-3}	7.82	2.870×10^{-3}	3.47	1.270×10^{-1}	3.77	4.210×10^{-2}	2.32
	1/8	2.650×10^{-3}	1.53	8.130×10^{-4}	1.82	8.260×10^{-2}	0.63	2.320×10^{-2}	0.86
	1/16	9.190×10^{-4}	1.53	2.130×10^{-4}	1.93	5.540×10^{-2}	0.58	1.250×10^{-2}	0.89
	1/32	3.260×10^{-4}	1.50	6.030×10^{-5}	1.82	3.920×10^{-2}	0.50	6.550×10^{-3}	0.93
iii. DG+SL	1/2	2.570×10^{-2}	–	7.330×10^{-3}	–	2.300×10^{-1}	–	7.160×10^{-2}	–
	1/4	7.620×10^{-3}	1.75	2.870×10^{-3}	1.35	1.270×10^{-1}	0.85	4.210×10^{-2}	0.77
	1/8	2.650×10^{-3}	1.53	8.130×10^{-4}	1.82	8.260×10^{-2}	0.63	2.320×10^{-2}	0.86
	1/16	9.190×10^{-4}	1.53	2.130×10^{-4}	1.93	5.540×10^{-2}	0.58	1.250×10^{-2}	0.89
	1/32	3.260×10^{-4}	1.50	6.030×10^{-5}	1.82	3.920×10^{-2}	0.50	6.550×10^{-3}	0.93
iv. DG+FL	1/2	$1.720 \times 10^{+0}$	–	3.210×10^{-2}	–	$1.720 \times 10^{+0}$	–	2.120×10^{-1}	–
	1/4	5.370×10^{-4}	11.64	3.000×10^{-3}	3.42	4.320×10^{-3}	8.64	4.250×10^{-2}	2.32
	1/8	1.730×10^{-4}	1.63	8.690×10^{-4}	1.79	1.840×10^{-3}	1.23	2.320×10^{-2}	0.87
	1/16	4.630×10^{-5}	1.90	2.300×10^{-4}	1.92	8.370×10^{-4}	1.13	1.250×10^{-2}	0.90
	1/32	1.180×10^{-5}	1.98	5.910×10^{-5}	1.96	4.100×10^{-4}	1.03	6.490×10^{-3}	0.94

Table 2
One-dimensional Buckley–Leverett problem: errors in L^2 and H^1 norms and convergence rates, for $\tau = O(h^2)$ and $t = 800$ days. Note that flux limiter algorithm preserves the accuracy of the DG discretization. However, slope limiter slightly degrades the rates of convergence.

	h (m)	τ (days)	$\|\|S_n - S(T)\|\|_{L^2(\Omega)}$	Rate	$\|\|S_n - S(T)\|\|_{H^1(\Omega)}$	Rate
i. DG	12	22.2	7.10×10^{-05}	–	8.39×10^{-04}	–
	6	5.05	3.09×10^{-05}	1.20	3.92×10^{-04}	1.10
	3	1.38	9.51×10^{-06}	1.70	2.25×10^{-04}	0.80
	1.5	0.345	2.57×10^{-06}	1.89	1.06×10^{-04}	1.09
	0.75	0.086	6.37×10^{-07}	2.01	5.28×10^{-05}	1.00
ii. DG+FL+SL	12	22.2	1.63×10^{-03}	–	1.23×10^{-02}	–
	6	5.05	1.65×10^{-04}	3.30	1.46×10^{-04}	6.40
	3	1.38	5.31×10^{-05}	1.64	9.42×10^{-05}	0.63
	1.5	0.345	1.43×10^{-05}	1.89	5.60×10^{-05}	0.75
	0.75	0.086	3.81×10^{-06}	1.91	3.24×10^{-05}	0.79
iii. DG+SL	12	22.2	3.70×10^{-04}	–	2.31×10^{-03}	–
	6	5.05	1.61×10^{-04}	1.20	1.08×10^{-03}	1.10
	3	1.38	5.17×10^{-05}	1.64	6.96×10^{-04}	0.63
	1.5	0.345	1.39×10^{-05}	1.89	4.14×10^{-04}	0.75
	0.75	0.086	3.71×10^{-06}	1.91	2.39×10^{-04}	0.79
iv. DG+FL	12	22.2	1.63×10^{-03}	–	1.28×10^{-02}	–
	6	5.05	2.18×10^{-04}	2.90	7.48×10^{-04}	4.10
	3	1.38	7.25×10^{-05}	1.59	4.51×10^{-04}	0.73
	1.5	0.345	1.89×10^{-05}	1.87	2.37×10^{-04}	0.93
	0.75	0.086	4.96×10^{-06}	2.00	1.18×10^{-04}	1.01

boundary. Dirichlet boundary conditions are: $P = 3 \times 10^6$ Pa and $S = 0.85$ on $\{0\} \times (0, 100)$; and $P = 10^6$ Pa on $\{100\} \times (0, 100)$ m. Outflow boundary condition is chosen for saturation on the right boundary and remaining boundaries are set as no-flow ($j^s = j^p = 0$). The pictorial descriptions of the pressure-driven flow problem are provided in Fig. 4.

Table 3
Problem constructed by the method of manufactured solution: errors and rates for the cell average values of saturation $\bar{S}$. The time step τ is set to h^2 and L^2 norms are computed at the final time $T = 1$. DG approximation with limiters return optimal convergence rate with respect to average values.

	h	$\|\|\bar{S}_n - \bar{S}(T)\|\|_{L^2(\Omega)}$	Rate
DG	1/2	5.900×10^{-4}	–
	1/4	4.839×10^{-4}	0.286
	1/8	1.661×10^{-4}	1.543
	1/16	4.506×10^{-5}	1.882
	1/32	1.148×10^{-5}	1.973
DG+FL+SL	1/2	$1.721 \times 10^{+0}$	–
	1/4	4.861×10^{-4}	11.790
	1/8	1.658×10^{-4}	1.552
	1/16	4.467×10^{-5}	1.892
	1/32	1.142×10^{-5}	1.967

Table 4
One-dimensional Buckley–Leverett problem: errors and rates for the cell average values of saturation $\bar{S}$. L^2 norms are computed for $\tau = O(h^2)$ at the final time $t = 800$ days. DG approximation with limiters return optimal convergence rate with respect to average values.

	h (m)	$\|\|\bar{S}_n - \bar{S}(T)\|\|_{L^2(\Omega)}$	Rate
DG	12	6.12×10^{-5}	–
	6	4.02×10^{-5}	0.601
	3	1.315×10^{-5}	1.606
	1.5	3.421×10^{-6}	1.950
	0.75	8.66×10^{-7}	1.982
DG+FL+SL	12	1.303×10^{-3}	–
	6	2.180×10^{-5}	5.901
	3	6.998×10^{-6}	1.643
	1.5	1.840×10^{-6}	1.923
	0.75	4.659×10^{-7}	1.987

4.2.1. Homogeneous domain

A homogeneous test problem with constant permeability of $K = 10^{-8}$ m^2 is examined here, with similar setup and parameters as in the work of Epshteyn and Riviere [13]. Relative permeabilities and capillary pressure are defined in Eqs. (4.4) and (4.8), respectively, with entry pressure $p_d = 1000$ Pa, $\theta = 2$ and $R = 0.05$. The viscosities are $\mu_w = 10^{-3}$ Pa s and $\mu_\ell = 10^{-2}$ Pa s. Two quadrilateral meshes are considered: (i) a uniform mesh with size of $h = 1.25$ m and (ii) a non-uniform mesh with 256 elements and with size of $h_{\text{bnd}} = 1.25$ m at the left boundary and $h = 6.583$ m for the rest of domain (see Fig. 5(a)). It is known that slope limiters by design flatten steep slopes near discontinuities (e.g., at left-most elements when simulation starts). Using a mesh with increased density at the (left) boundary reduces the effect of overflattening on the accuracy of solutions [73,74]. The time step is chosen as $\tau = 0.2$ s, the final time is $T = 300$ s, and the penalty parameter is $\sigma = 100$. We compare our numerical solutions with a reference unlimited solution obtained from the fully implicit DG formulation developed by Epshteyn and Riviere [13] on a quadrilateral mesh with 256 elements. The saturation and pressure profiles obtained with our proposed scheme, along the line $y = 50$ m are illustrated in Figs. 6(a) and 6(b). Numerical solutions, compared to reference solution, are accurate and in good agreement with respect to front location. As expected, the finer mesh tracks the saturation front with more accuracy. It is also evident that our limiting scheme successfully yields pointwise bound-preserving and monotone solutions. However, the reference solution unsurprisingly violates undershoot bound (about 4% right after the saturation front) and produces an oscillatory saturation profile.

To better understand the efficacy of the proposed limiting algorithm (i.e., DG+SL+FL), and distinguish it from the vertex-based slope limiter of Kuzmin [25] (i.e., DG+SL), we solve the problem again (with same parameters as

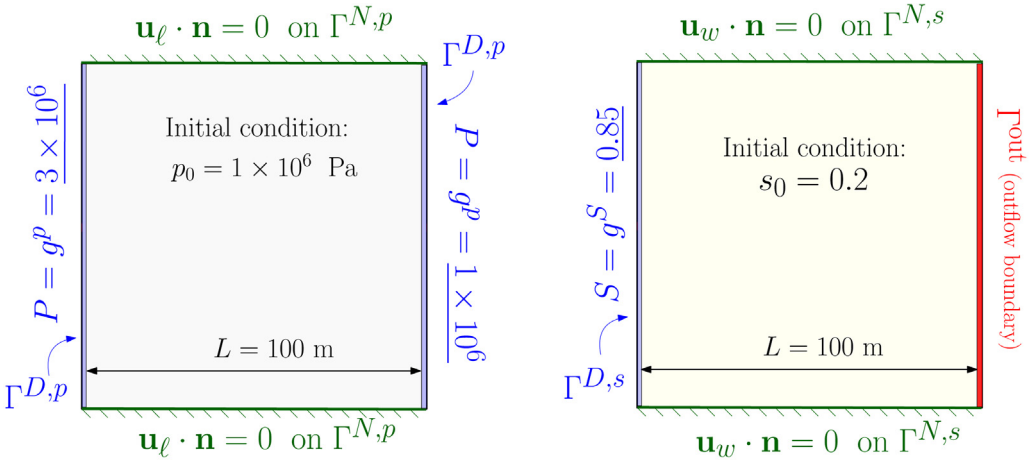

(a) Boundary condition for pressure (b) Boundary condition for saturation

Fig. 4. Two-dimensional pressure-driven flow problem: This figure provides a pictorial description of the computational domain and boundary value problem.

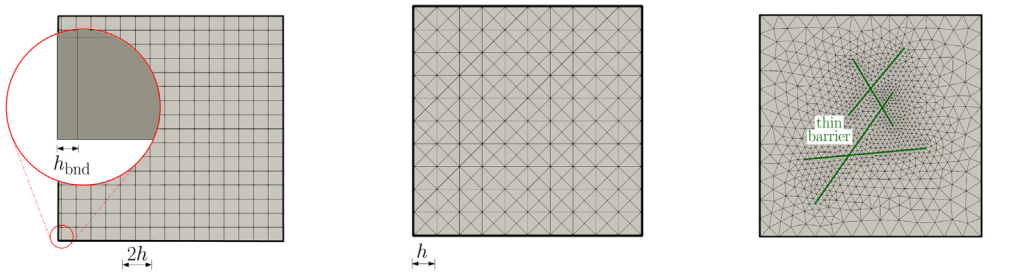

(a) Quadrilateral mesh (b) Crossed trianglular mesh (c) Mesh for thin-barrier problem

Fig. 5. Two-dimensional pressure-driven flow problem: This figure shows the typical meshes employed in our numerical simulations.

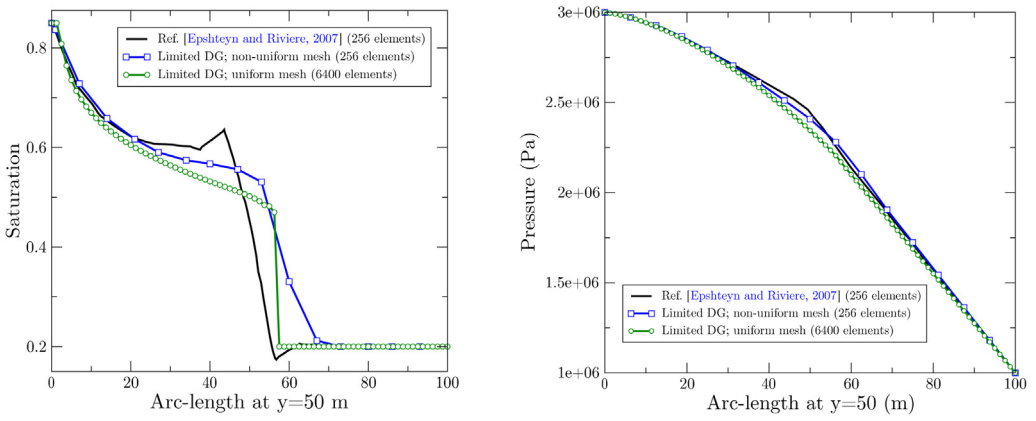

(a) Saturation profile (b) Pressure profile

Fig. 6. Two-dimensional pressure-driven flow in homogeneous domain: This figure exhibits the saturation and pressure profiles obtained from limited DG approximations (with $\mathbb{P} = 1$ and $\sigma = 100$). Solutions on uniform and non-uniform meshes are plotted along the line $y = 50$ m at $t = 300$ s and are compared with a reference DG solution. Regardless of the mesh size, limiters completely suppress unphysical overshoots and undershoots and accurately predict the location of saturation front which is in good agreement with that of the reference solution. As expected, the uniform finer mesh gives rise to a sharper front. On the other hand, the reference solution is not equipped with any bound-preserving mechanism and thus does not enjoy maximum principle and lower bound violations ($S < 0.2$) and non-monotone behavior are captured.

Table 5
This table shows the efficacy of the limiters when applied to the pressure-driven flow problem with homogeneous domain. Simulations are carried out for the duration of 450 s on crossed mesh (see Fig. 5(b)) for different mesh-sizes. In this table, max $\mathcal{M}$ denotes the maximum magnitude value of local mass balance error observed for all time steps.

Mesh-size (m)	Algorithm	Max undershoot	Max undershoot (%)	Max overshoot	Max overshoot (%)	Max $\mathcal{M}$	Monotonocity
$h = 10$	DG	−0.109	47.61	0.854	0.56	1.37×10^{-15}	✗
	DG+SL	0.169	4.79	0.85	0	2.23×10^{-9}	✗
	DG+FL+SL	0.2	0	0.85	0	7.66×10^{-12}	✓
$h = 5$	DG	−0.093	45.13	0.852	0.28	5.41×10^{-15}	✗
	DG+SL	0.169	4.78	0.85	0	3.24×10^{-9}	✗
	DG+FL+SL	0.2	0	0.85	0	7.03×10^{-11}	✓
$h = 2.5$	DG	−0.059	40	0.851	0.136	2.19×10^{-14}	✗
	DG+SL	0.172	4.29	0.85	0	2.57×10^{-8}	✗
	DG+FL+SL	0.2	0	0.85	0	2.22×10^{-14}	✓
$h = 1.25$	DG	0.010	29.21	0.8502	0.07	9.78×10^{-14}	✗
	DG+SL	0.178	3.32	0.85	0	2.57×10^{-7}	✗
	DG+FL+SL	0.2	0	0.85	0	1.08×10^{-13}	✓

Table 6
This table shows the range of number of Newton iterations and flux limiter iterations for three different mesh types of crossed triangular, quadrilateral, and structured triangular with right diagonals. Proposed post-processing limiters (applied after each time step) do not alter the Newton's solver performance for all meshes. However, maximum number of flux limiter iterations increases for finer meshes.

h (m)	Unlimited DG			Limited DG					
	Newton's iter.			Newton's iter.			Flux limiter's iter.		
	Crossed mesh	Quad. mesh	Trig. mesh	Crossed mesh	Quad. mesh	Trig. mesh	Crossed mesh	Quad. mesh	Trig. mesh
10	3–4	3–4	3–4	3–4	3–4	3–4	1–25	1–9	1–26
5	3–4	3–4	3–4	3–4	3–4	3–4	1–55	1–19	1–46
2.5	3–4	3–4	3–4	3–4	3–4	3–4	1–116	1–38	1–79
1.25	3–4	3–4	3–4	3–4	3–4	3–4	1–238	1–78	1–159

before) on a crossed structured mesh (shown in Fig. 5(b)) for total duration of $T = 450$ s. The initial size of $h = 10$ m is chosen for this analysis and four-step refinement is performed. Table 5 reports the performance of limiters and compare them with respect to bound-preserving properties, local mass balance violations, and monotonocity. We observe that mesh refinement reduces maximum undershoots of unlimited DG from 47.61% to 29.21% and maximum overshoots to less than 0.1% but does not eliminate violations. The application of slope limiter to DG eliminates undershoots at all time steps and significantly reduces maximum overshoots to 4.79% for the coarsest mesh and to 3.32% for the finest mesh. It can be seen that DG+SL falls short to satisfy maximum principle even under excessive mesh refinement. Further, it should be noted that both DG and DG+SL approximations fail to obtain monotone solutions near the saturation front. This means that they are susceptible to local spurious oscillations near the front even when the global bounds are not violated. However, approximations under DG+FL+SL enjoy pointwise maximum principle and the saturation field remain monotone over the entire domain, independently of the mesh size.

As shown in Table 6, a few Newton iterations are needed at each time step for the convergence of either limited DG or unlimited DG approximations for three different mesh types. Results suggest that the limiters do not have a significant effect on the number of solver iterations, regardless of mesh size and type. We also see that the maximum number of flux limiter iterations increases as we refine the mesh. It should be noted that the reported number range is collected throughout all time steps of simulation and we observed that in fact for most time steps (over 85% to 90%), flux limiter iterations remain relatively small (less than 5) regardless of the size and the type of the mesh.

4.2.2. Local mass balance

DG methods are known for their local mass conservation properties. [75,76]. In this section, we investigate the effect of the proposed limiters on altering local mass conservation properties. Upon applying element-wise averages

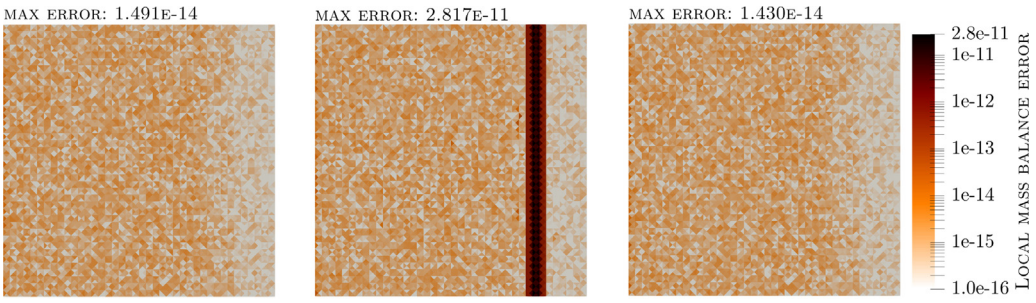

(a) DG with no limiter (b) DG+SL (c) DG+FL+SL

Fig. 7. Local mass balance conservation for pressure-driven flow problem: This figure shows the local mass conservation properties of the limited and unlimited DG approximations on a homogeneous domain with $h = 2.5$ m at $t = 450$ s. DG+SL near the front induces slight increase in mass balance error but, overall errors remain small for all three cases.

and choosing unit test function in (3.4), we obtain the local mass conservation of an element $E \in \mathcal{E}_h$ at time t_n:

$$\mathcal{M}(E) = \frac{\phi(\bar{S}_{n+1}|_E - \bar{S}_n|_E)}{\tau} + \frac{1}{|E|}\sum_{e\subset\partial E}\mathcal{H}_{n+1,E}(e) - \left(f_w(s_{\text{in}})\bar{q}_E - \overline{f_w(S_n|_E)}\underline{q}_E\right). \tag{4.9}$$

We compute the magnitude of mass balance error for the pressure-driven flow problem discussed in the previous section. Table 5 contains the value of maximum error observed throughout the simulation. Evidently, DG+SL scheme is slightly worse than other two schemes with respect to errors, which is consistent for all mesh-sizes. However, values are all very small and below than the solver tolerance. In Fig. 7, the values of $\mathcal{M}(E)$ are displayed at $t = 450$ s on a crossed mesh of size $h = 2.5$ m for three cases of DG, DG+SL, and DG+FL+SL. One can see that applying slope limiter (without flux limiter) instigates an erroneous patch (shown with dark brown color in Fig. 7(b)). It is also clear that the proposed numerical scheme (i.e., DG+FL+SL) is locally mass conservative and slightly outperforms DG+SL scheme.

4.2.3. Domain with thin barrier

In this example, the porous medium contains a thin barrier and it is partitioned into an unstructured triangular mesh (see Fig. 5(c)). Total time is set to $T = 4500$ s and the time step is $t = 0.5$ s. Additionally, noflow boundary conditions are imposed on the barrier edges. All other parameters are the same as in Section 4.2.1. Fig. 8 exhibits the saturation profile under limited and unlimited DG at three different time steps. Limited DG, unlike its unlimited version, generates saturation that remains bounded and neither undershoots (blue-colored cells) nor overshoots (red-colored cells) are detected during the simulation. Nonetheless, the saturation front, under both unlimited and limited DG, propagates with the same speed and tends to avoids the barrier as expected. Figs. 9 and 10 show the wetting phase pressure contour and velocity field at $t = 4500$ s. Velocities are computed at time t_n, using the formula: $\mathbf{u}_w^n = -K\lambda_w(S_n)\nabla P_n$. We can see that pressure drops linearly near the top and bottom edges, which confirms that fluid steers clear of the central barrier and flows around it. When no limiter is used, spurious oscillations and erroneous high-velocity regions are visible in velocity solutions. Limited DG, on the other hand, gives very smooth approximations. From these results we conclude that the proposed numerical scheme is bound-preserving on unstructured meshes.

4.2.4. Non-homogeneous domain

For this problem, permeability is 10^{-8} m^2 everywhere except inside a square inclusion of length 20 m located at the center of the domain, where the permeability is 10^4 times smaller. The domain is discretized with a structured rectangular mesh of size $h = 1.25$ m. Time step is set to $\tau = 0.5$ s and the simulation advances up to $T = 650$ s. The remaining parameters are the same as in Section 4.2.1. The capillary pressure and phase mobilities are defined by (4.4) and (4.8) with $p_d = 1000$ Pa, $\theta = 2$ and $R = 0.05$ for the entire domain. The discrete saturation at different snapshots of $t = 350$ and $t = 650$ s is depicted in Fig. 11, where saturation values beyond the physical bounds (i.e., $S > 0.85$ and $S < 0.2$) are clipped away. Evidently, no matter if limiters are used or not, the injected

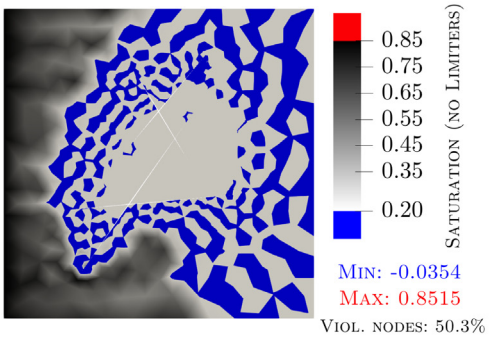

(a) DG with no limiter; $t = 250$ s

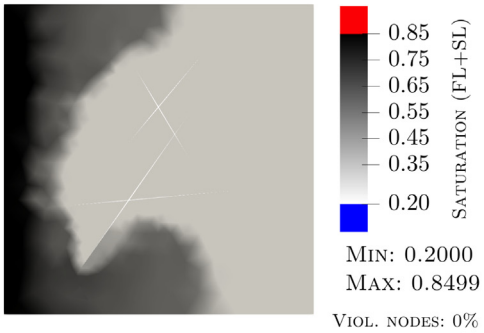

(b) DG+FL+SL; 250 s

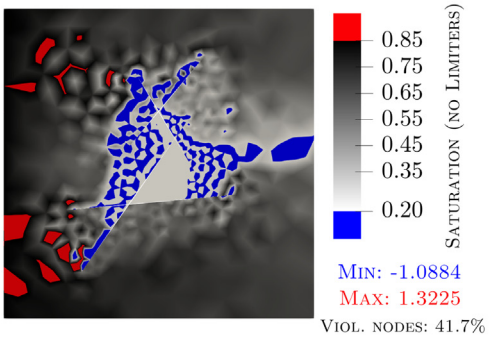

(c) DG with no limiters; $t = 1000$ s

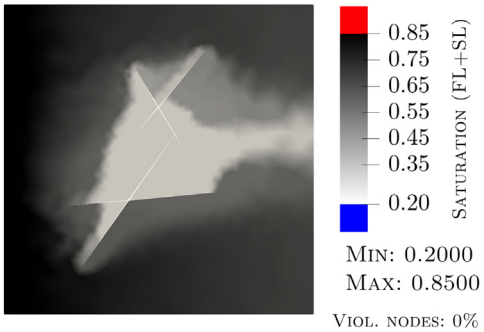

(d) DG+FL+SL; $t = 1000$ s

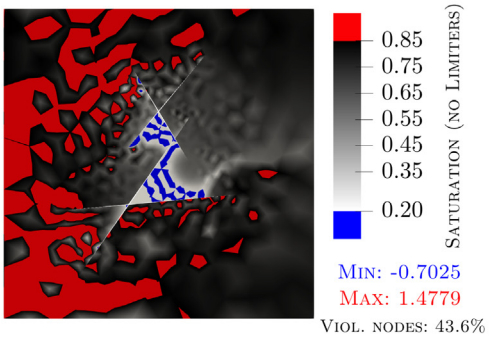

(e) DG with no limiters; $t = 4500$ s

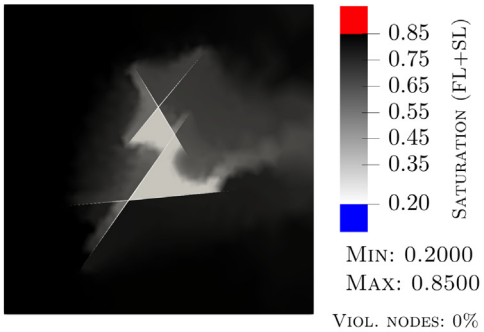

(f) DG+FL+SL; $t = 4500$ s

Fig. 8. Homogeneous domain with thin barrier: This figure shows the evolution of saturation profile using DG scheme without limiter (left) and with the proposed limiters (right). The color mapping for S in $[0.2, 0.85]$ is grayscale, while values below and above bounds are colored blue and red, respectively. As expected, DG approximation with no limiter yields noticeable violations, while limited DG scheme is capable of providing maximum-principle satisfying results. In spite of this, the front under both unlimited and limited DG, propagates with the same speed. (For interpretation of the references to color in this figure legend, the reader is referred to the web version of this article.)

wetting phase travels from left to right while avoiding the region of lower permeability. Both limited and unlimited schemes generate sharp and consistent saturation fronts. However, without limiter, the DG scheme presents strong oscillations behind and ahead of the inclusion. When limiters are activated, oscillations are suppressed and solutions are free of undershoots/overshoots.

Figs. 12 and 13 depict the pressure and velocity solutions, respectively, computed at $t = 650$ s by the DG formulation with limiter and without limiter. Limiting scheme has minimal effect on the pressure but this is not the

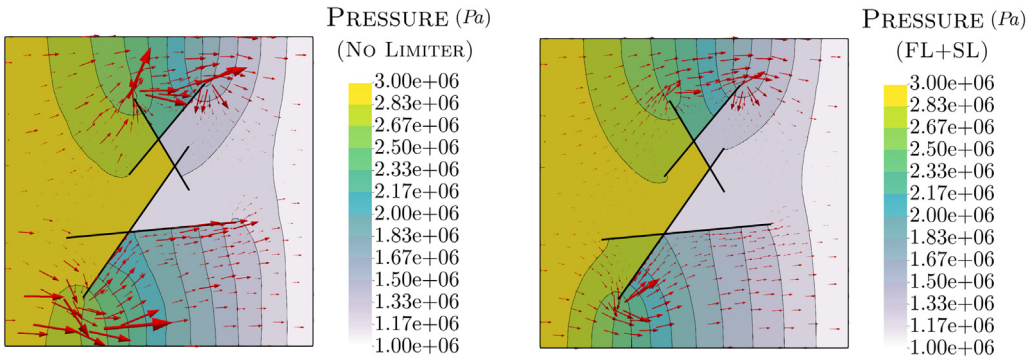

(a) DG with not limiter (b) DG+FL+SL

Fig. 9. Homogeneous domain with thin barrier: This figure depicts the pressure solutions at final time $t = 4500$ s using DG scheme (a) without limiter and (b) with limiters. The color contours represent the wetting phase pressure and the red arrows represent the velocity field. The length of the arrows scales with the magnitude of velocity. For both cases, flow goes around the impassible barrier and pressure linearly drops near top and bottom channels. (For interpretation of the references to color in this figure legend, the reader is referred to the web version of this article.)

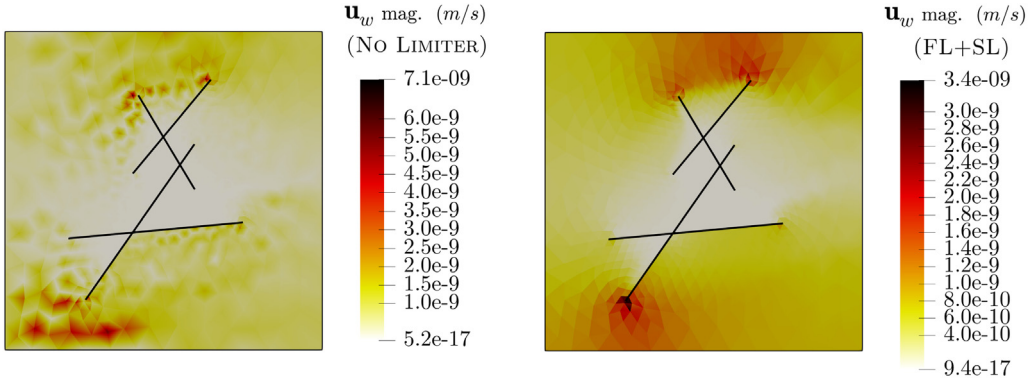

(a) DG with no limiter (b) DG+FL+SL

Fig. 10. Homogeneous domain with thin barrier: This figure shows the magnitude of wetting phase velocity at final time $t = 4500$ s using DG scheme (a) without limiter and (b) with limiters. The main inference from this figure is that when no limiter is used (a), DG approximation induces overestimation and spurious oscillations in velocity field. The proposed limiting scheme mitigates this issue and yields smooth solutions (b).

case for the velocity. Velocities obtained under DG with no limiter exhibit spurious oscillations, which resemble those in saturation profile. On the other hand, the limiting scheme eliminates oscillations in the velocity field.

4.3. Quarter five-spot problem

In this section, the performance and robustness of the limiters are assessed in the presence of wells, for both homogeneous and heterogeneous permeabilities. We employ no flow boundary condition on the entire boundary, as shown in Fig. 14; and assume zero capillary pressure. The flow is driven from an injection well at the bottom left corner to a production well at the top right corner. The wells are defined by source/sink terms, which are piecewise constant with compact support. That is, $\bar{q}$ is nonzero at injection well and $\underline{q}$ is nonzero at production well. The DG penalty parameters for test problems are taken as $\sigma = 10$.

4.3.1. Homogeneous domain

The domain $\Omega = [0, 100]^2$ m^2 is partitioned into a crossed structured mesh of size $h = 2.5$ m, as depicted in Fig. 5(b). The medium is homogeneous with $K = 10^{-13}$ m^2 everywhere. We choose Brooks–Corey relative

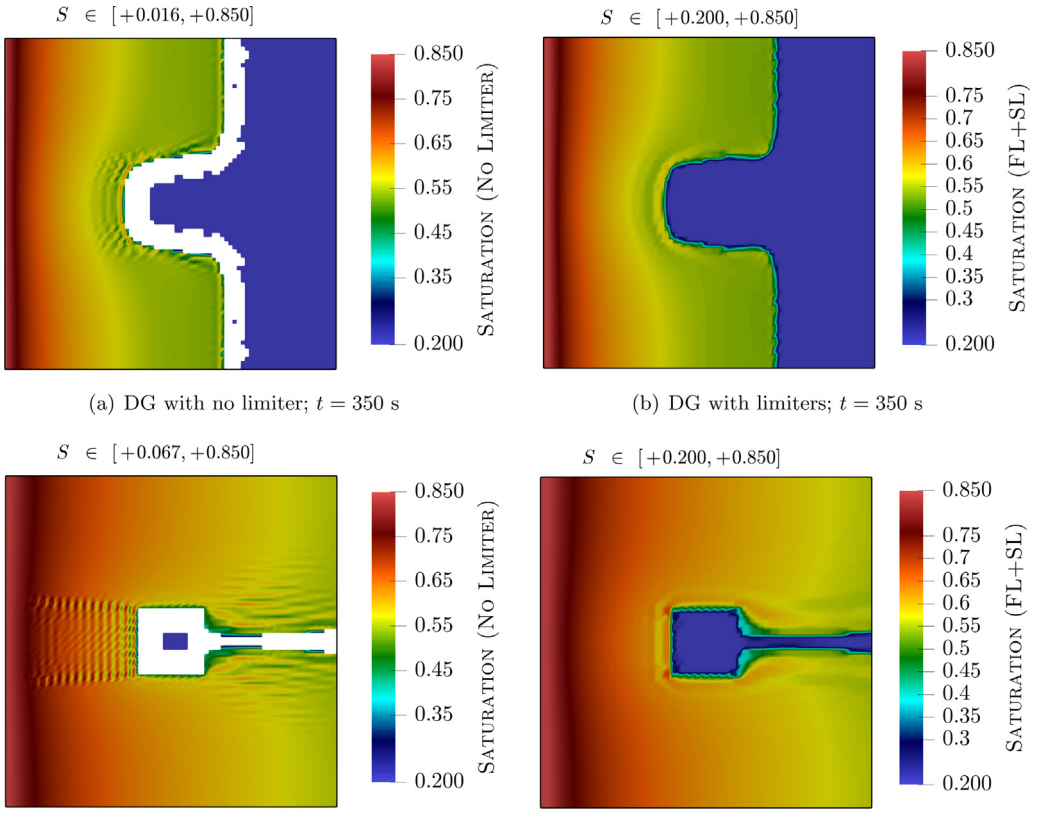

(a) DG with no limiter; $t = 350$ s

(b) DG with limiters; $t = 350$ s

(c) DG with no limiter; $t = 650$ s

(d) DG with limiters; $t = 650$ s

Fig. 11. Non-homogeneous pressure-driven flow problem: This figure shows saturation fields obtained with DG (left) and with DG+FL+SL (right). Values beyond the physical bounds (i.e., $S > 0.85$ and $S < 0.2$) are clipped away using tolerance 10^{-5}. Using either scheme, the wetting phase does not flood the inclusion and saturation fronts remain sharp and propagate similarly. Notice that spurious oscillations and violations of the physical constraints occur under the DG formulation but not under the limited DG.

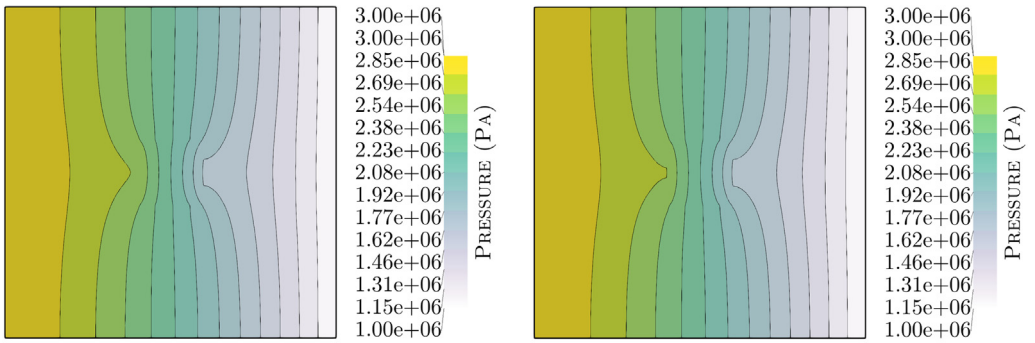

(a) DG; $t = 650$

(b) DG+FL+SL; $t = 650$

Fig. 12. Non-homogeneous pressure-driven flow problem: This figure shows pressure at final time $t = 650$ s using DG scheme (a) without limiter and (b) with limiter.

permeabilities as follows:

$$k_{rw}(s_e) = s_e^2, \quad k_{r\ell}(s_e) = (1 - s_e)^2, \quad s_e = \frac{S - s_{rw}}{1 - s_{rw} - s_{r\ell}}. \tag{4.10}$$

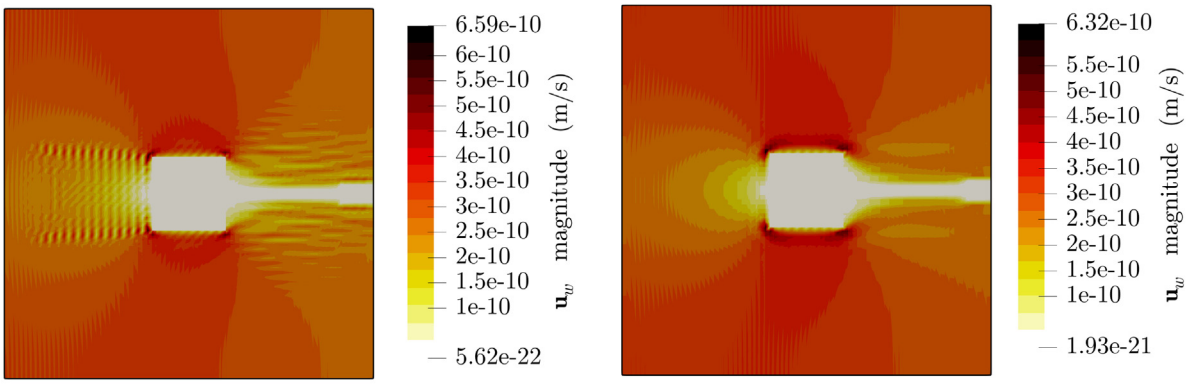

(a) DG; $t = 650$ (b) DG+FL+SL; $t = 650$

Fig. 13. Two-dimensional pressure-driven flow problem: This figure shows the magnitude of wetting phase velocity at final time $t = 650$ s using DG scheme (a) without limiter and (b) with limiter. In the unlimited case, oscillations earlier observed in saturation are reflected in the velocity field. However, with limiters, oscillations are eliminated.

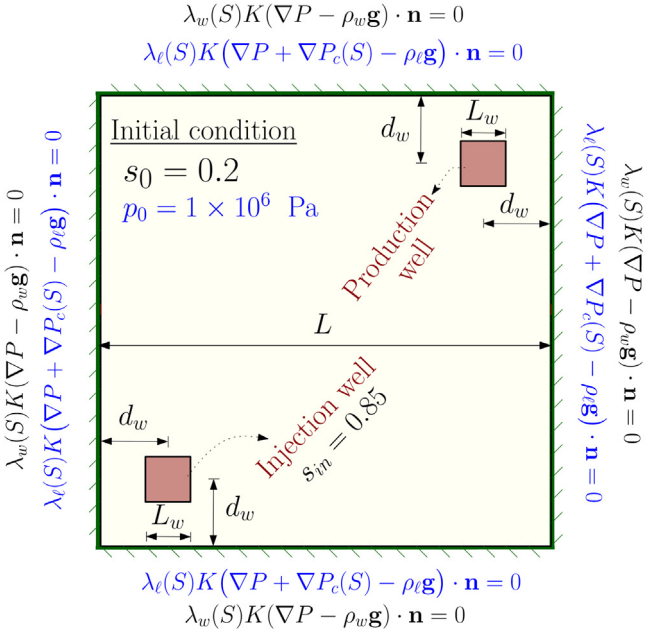

Fig. 14. Quarter five-spot problem: This figure provides a pictorial description and the boundary value problem. No flow boundary conditions are prescribed on the entire boundary.

The injection and production flow rates of wells are determined by the following constraint:

$$\int_\Omega \bar{q} = \int_\Omega \underline{q} = 7.03125 \times 10^{-4}, \tag{4.11}$$

where $\bar{q}$ is piecewise constant on $[2.5, 10]^2$ m^2 and $\bar{q} = 0$ elsewhere and $\underline{q}$ is piecewise constant on $[90, 97.5]^2$ m^2 and $\underline{q} = 0$ elsewhere. The final time is $T = 21$ days and time step is $\tau = 0.057$ days.

Fig. 15 shows the wetting phase saturations at two different times ($t = 10$ and $t = 21$ days), for three schemes: DG, DG+SL, DG+FL+SL. The figure shows that violations of the maximum principle for the unlimited DG solution occur in the neighborhood of the injection well and after the front; in addition the DG solution is not monotone before the front. Adding a slope limiter helps with the monotonicity of the solution and with decreasing the number

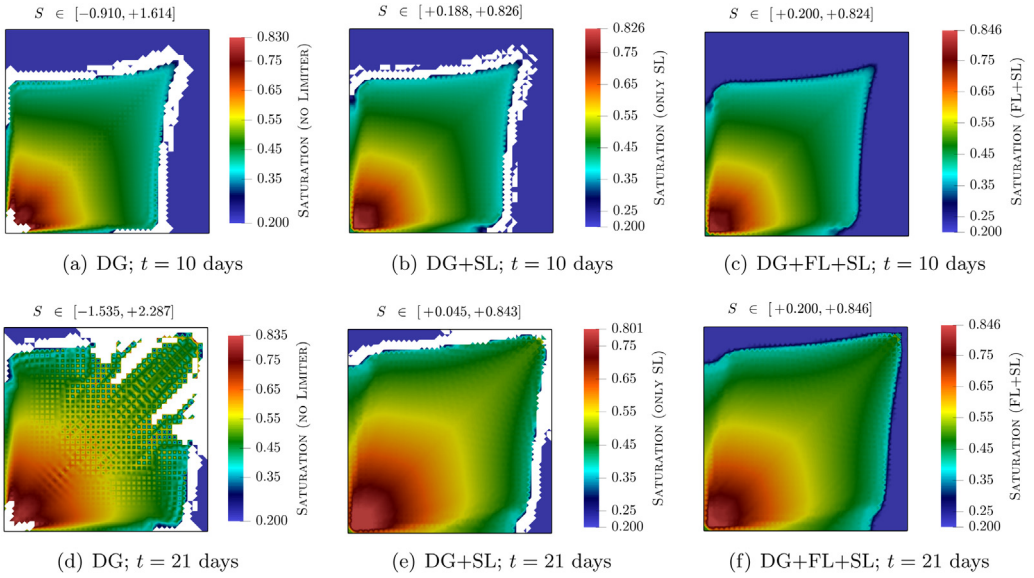

(a) DG; $t = 10$ days (b) DG+SL; $t = 10$ days (c) DG+FL+SL; $t = 10$ days

(d) DG; $t = 21$ days (e) DG+SL; $t = 21$ days (f) DG+FL+SL; $t = 21$ days

Fig. 15. Quarter five-spot problem with homogeneous permeability: This figure shows the saturation solutions obtained with DG (left), DG+SL (middle), and DG+FL+SL (right) at two different time steps. Values beyond the physical bounds (i.e., $S > 0.85$ and $S < 0.2$) are clipped away using tolerance 10^{-5}. This figure suggests that DG+FL+SL, unlike the two other schemes, provides maximum-principle satisfying results at all time steps.

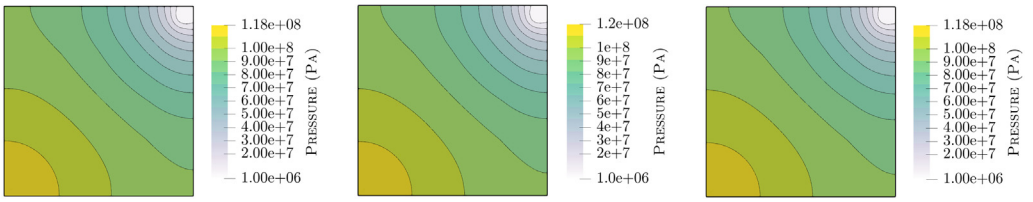

(a) DG (b) DG+SL (c) DG+FL+SL

Fig. 16. Quarter five-spot problem with homogeneous permeability: This figure shows the wetting phase pressure at final time $t = 10$ days using DG, DG+SL, and DG+FL+SL schemes. All three cases yield similar approximations.

of elements where the maximum principle is not satisfied. The proposed numerical scheme, DG+FL+SL, completely eliminates violation of maximum principle: the solution is monotone and bound-preserving. Figs. 16 and 17 show the wetting phase pressure contours and velocity fields at $t = 10$ days for all three cases. Differences are minimal for the pressure and velocity fields. Finally we display the local mass balance error in Fig. 18 for all three cases; the local mass balance error is a piecewise constant field $\mathcal{M}$ defined by (4.9). We observe that the error is negligible (of the order of 10^{-11}) for the DG scheme with or without limiters.

4.3.2. Quarter five-spot problem with heterogeneous domain

We repeat the experiments in Section 4.3.1 with heterogeneous medium of $\Omega = [0, 1000]^2$ m^2. The permeability fields are discontinuous and values vary over seven orders of magnitude. The permeability data is taken from two layers of the SPE 10 data-set [77]; and are scaled to a crossed structured mesh of size $h = 20$ m (see permeability fields in log-scale in Fig. 19). We note that layer 13 varies relatively smoothly, whereas layer 73 contains well-defined channels, which form an additional challenge for any numerical method. We set viscosities to $\mu_w = 5\times10^{-4}$ Pa s and $\mu_\ell = 2 \times 10^{-3}$ Pa s and invoke Brooks–Corey relative permeabilities as follows:

$$k_{rw}(s_e) = s_e^5, \quad k_{r\ell}(s_e) = (1 - s_e)^2(1 - s_e^5), \quad s_e = \frac{S - s_{rw}}{1 - s_{rw} - s_{r\ell}}. \tag{4.12}$$

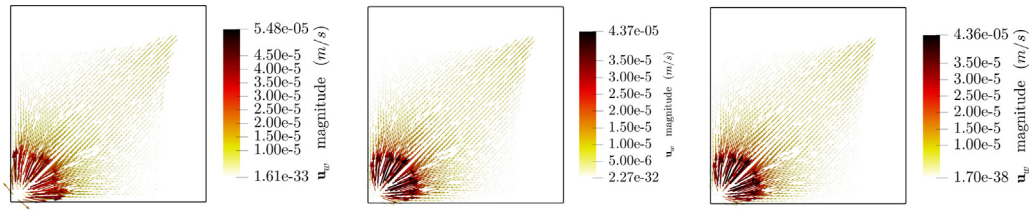

(a) DG (b) DG+SL (c) DG+FL+SL

Fig. 17. Quarter five-spot problem with homogeneous permeability: This figure depicts the wetting phase velocity at time $t = 10$ days using DG, DG+SL, and DG+FL+SL schemes. All three cases yield similar approximations.

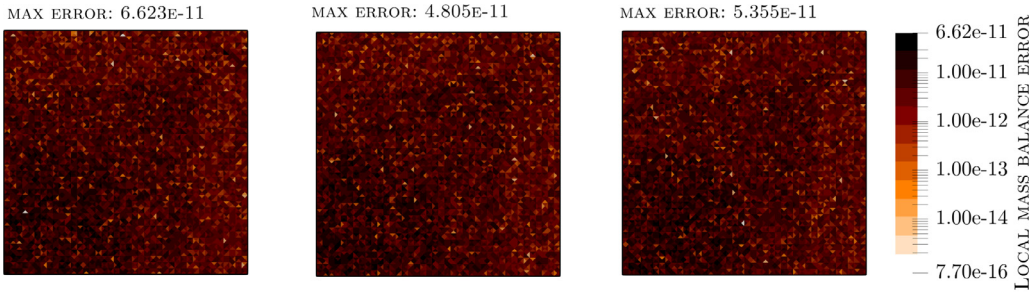

(a) DG (b) DG+SL (c) DG+FL+SL

Fig. 18. Local mass balance conservation for quarter five-spot problem: This figure illustrates the local mass balance error at time $t = 10$ days. No matter what scheme is used the errors always remain small (in the order of 10^{-11}).

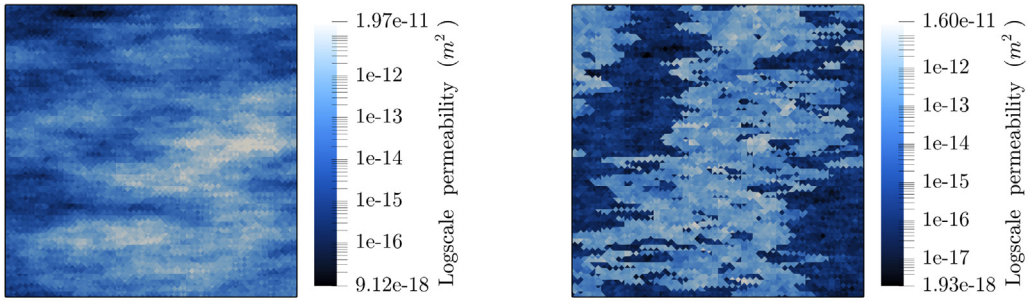

(a) layer 13 (b) layer 73

Fig. 19. Quarter five-spot problem with heterogeneous permeability: This figure illustrates the permeability fields adopted from two horizontal layers of SPE10 model 2 data-set. Layer 13 is taken from relatively smooth Tarbert formation, whereas layer 73 is taken from a highly varying Upper-Ness formation. Values are presented in logarithmic scale.

The production and injection wells of size $L_w = 100$ m with $\bar{q} = \underline{q} = 2.8 \times 10^{-5}$ are positioned at opposite corners such that $d_w = 70$ m (see Fig. 14). The time step is $\tau = 4.17 \times 10^{-3}$ days and the final time is $T = 1.375$ days.

We apply our proposed DG scheme with both flux and slope limiters to these porous media. Fig. 20 displays the wetting phase saturation contours at different times ($t = 0.417$, 0.83, 1.375 days) for both layers. As expected the wetting phase floods the domain from the injection well to the production well while avoiding low permeable regions. Because of the location of channels in layer 73, the wetting phase has reached the production well at

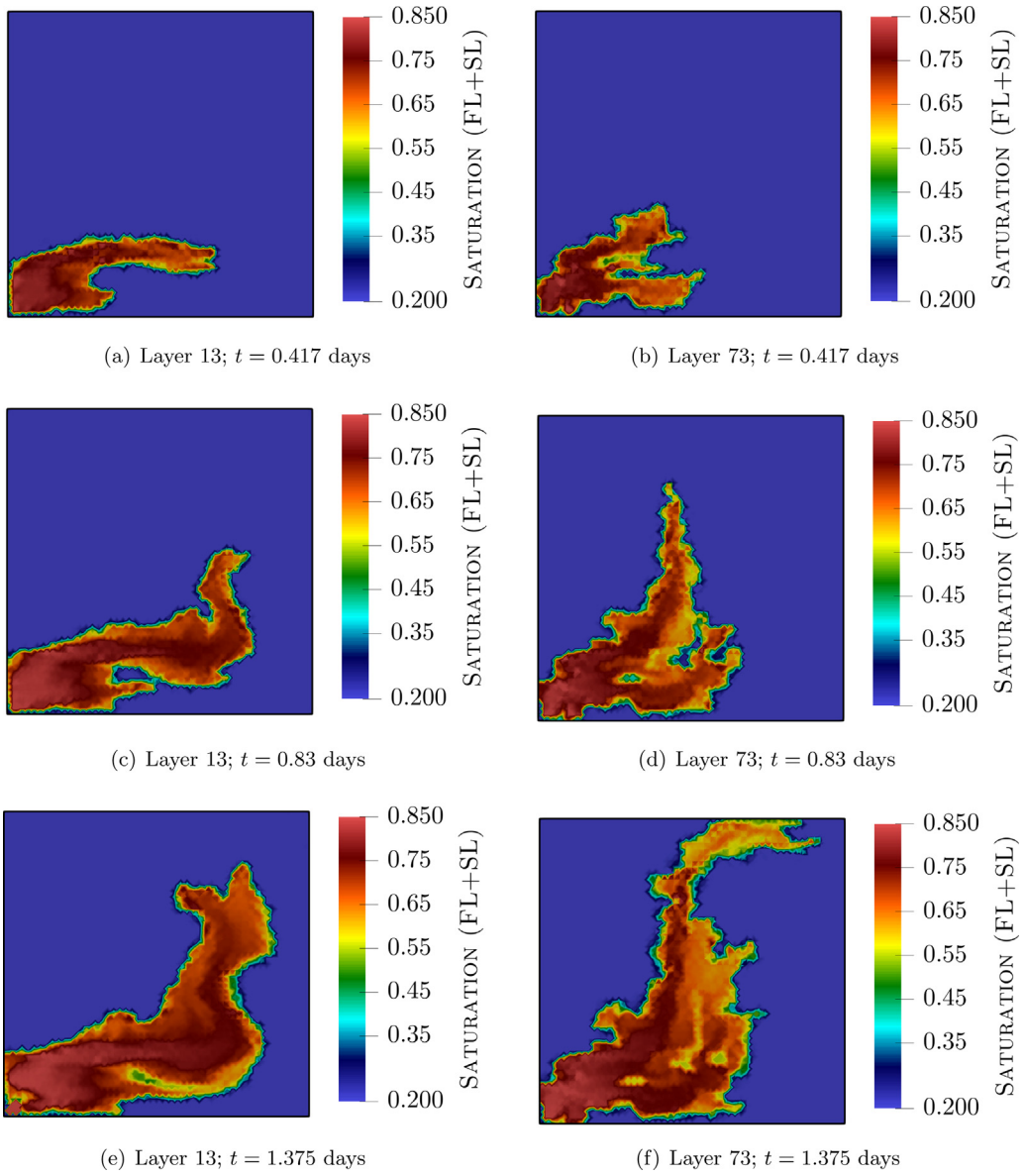

(a) Layer 13; $t = 0.417$ days

(b) Layer 73; $t = 0.417$ days

(c) Layer 13; $t = 0.83$ days

(d) Layer 73; $t = 0.83$ days

(e) Layer 13; $t = 1.375$ days

(f) Layer 73; $t = 1.375$ days

Fig. 20. Quarter five-spot problem with heterogeneous permeability: This figure shows the evolution of the saturation obtained using DG+FL+SL scheme for layer 13 (left) and layer 73 (right). For both cases, the wetting phase moves toward the production well by sweeping the regions with highest permeability values. Another inference is that proposed limiters yield physical values of saturation, without any overshoots and undershoots, even for domains with permeabilities that vary over several orders of magnitudes.

time $t = 1.375$ days whereas this is not the case for layer 13. We also observe that the saturation satisfies the maximum principle. Fig. 21 shows the magnitude of the wetting phase velocity at the same times. The effect of the heterogeneities can be seen in the velocity fields.

4.4. Effect of gravity

In this section, we examine the success of our limiting scheme in the presence of gravity field and then study the impact of gravity on the pressure-driven flows and quarter five-spot problems. The ratio of gravitational to viscous forces can be represented as a gravity number, Gr. This dimensionless parameter depends on the difference between

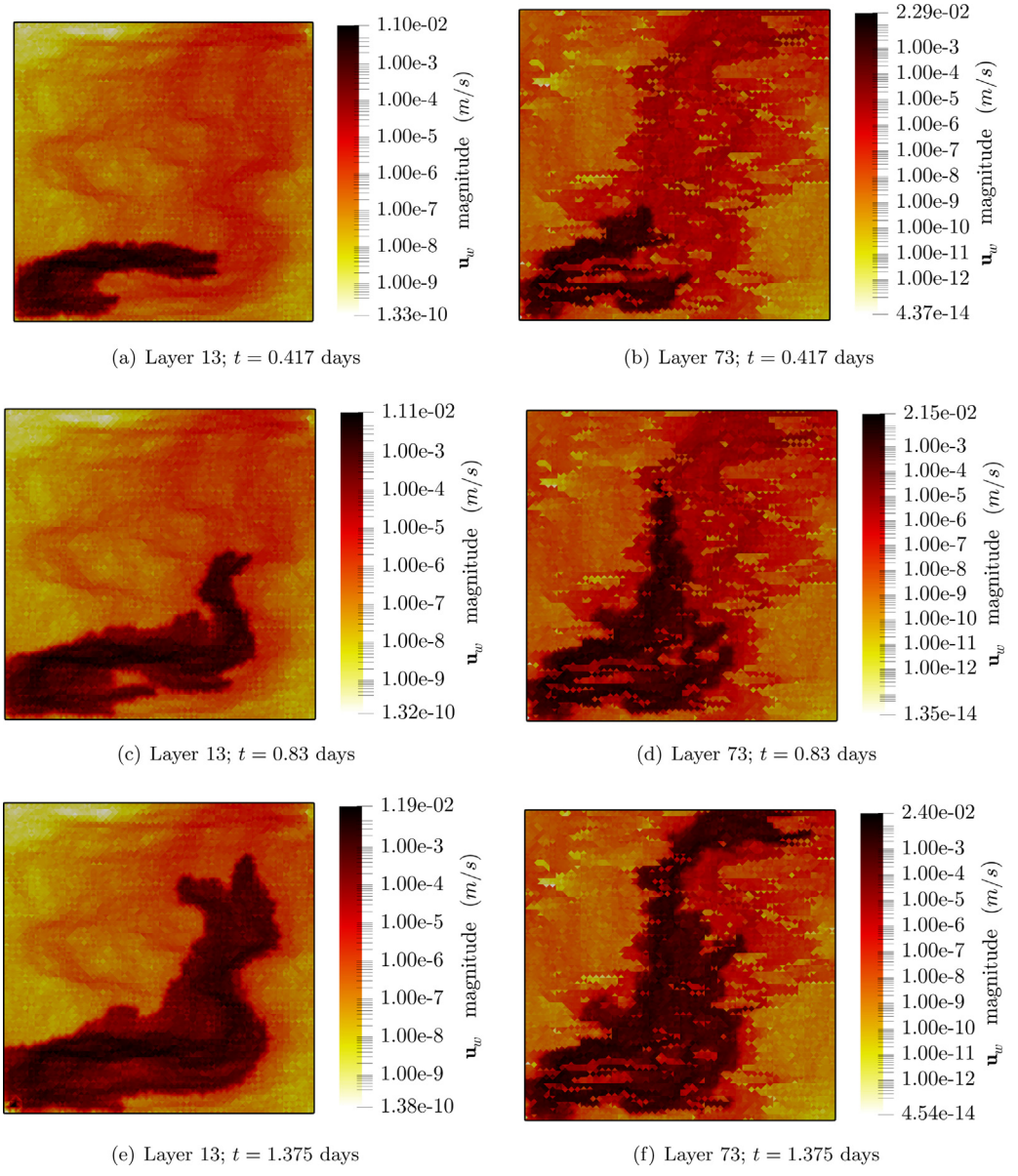

(a) Layer 13; $t = 0.417$ days

(b) Layer 73; $t = 0.417$ days

(c) Layer 13; $t = 0.83$ days

(d) Layer 73; $t = 0.83$ days

(e) Layer 13; $t = 1.375$ days

(f) Layer 73; $t = 1.375$ days

Fig. 21. Quarter five-spot problem with heterogeneous permeability: This figure shows the magnitude of wetting phase velocities obtained using DG+FL+SL for layer 13 (left) and layer 73 (right). The effect of heterogeneities is reflected in the velocity fields.

phase densities; and following the work of [78–80], can be defined as follows:

$$\mathrm{Gr} = \frac{K(\rho_w - \rho_\ell)g}{\mu_w U}, \tag{4.13}$$

where U is the characteristic magnitude of velocity.

4.4.1. Pressure-driven flows

The domain $\Omega = [0, 200] \times [0, 100]$ m^2 is partitioned into a crossed mesh with 7200 triangular elements. The viscosities are $\mu_w = 2.5 \times 10^{-4}$ Pa s and $\mu_\ell = 5 \times 10^{-3}$ Pa s. Here, the characteristic velocity is estimated to be $U \approx 0.1$ m/s (using $U \approx -K(P|_{x=200} - P|_{x=0})/\mu_w L$). The wetting phase density is $\rho_w = 1000$ kg/m^3 and the non-wetting phase density takes three different values $\rho_\ell = 925, 850, 600$ kg/m^3, which yields three values for the

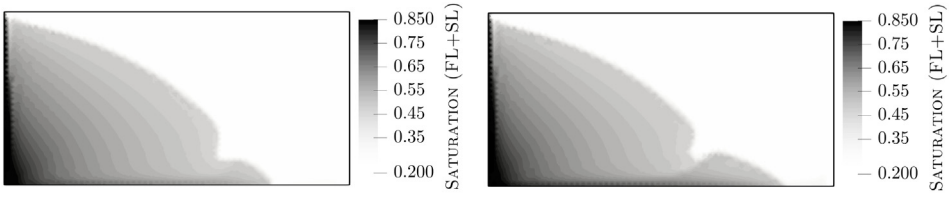

(a) Gr = 0.3 (b) Gr = 0.6

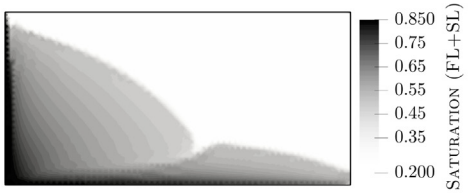

(c) Gr = 1.6

Fig. 22. Two-dimensional pressure-driven flow problem with gravity field: This figure shows the wetting phase saturation solutions at $t = 600$ s for different gravity numbers. Both flux and slope limiters are used. As the gravity number increases, more wetting phase accumulates at the bottom of the domain. For all three cases, no violation of maximum principle is observed.

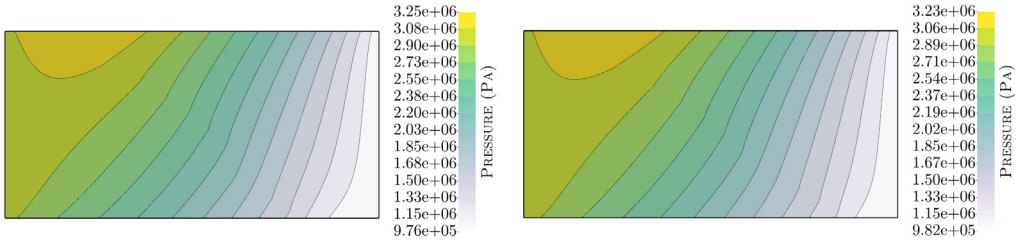

(a) Gr = 0.3 (b) Gr = 0.6

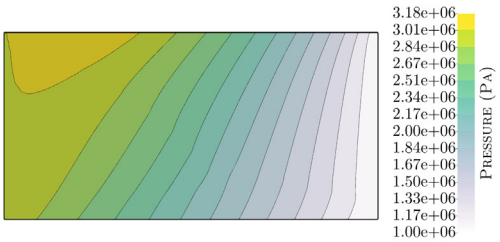

(c) Gr = 1.6

Fig. 23. Two-dimensional pressure-driven flow problem with gravity field: This figure shows the wetting phase pressure solutions at $t = 600$ s for different gravity numbers.

gravity number Gr= 0.3, 0.6 and 1.6 respectively. Other parameters and Dirichlet boundary conditions are the same as in Section 4.2.1. The time step is $\tau = 0.6$ s and the final time is $T = 600$ s. The proposed DG scheme with flux and slope limiters is applied and the penalty parameter is set to $\sigma = 1000$. Fig. 22 shows the saturation contours at the time $t = 600$ s. As the gravity number increases, the wetting phase saturation, which is the heaviest, deposits more and more at the bottom of the domain; and the narrow gravity tongue along the bottom edge becomes more pronounced. It should be also noted that similar to earlier problems, the limiting scheme exhibits satisfactory results with respect to the maximum principle. This means that for all three cases, solutions always remain between 0.2 and 0.85. Pressure contours and velocity fields are displayed in Figs. 23 and 24. Both show the impact of gravity on the solutions.

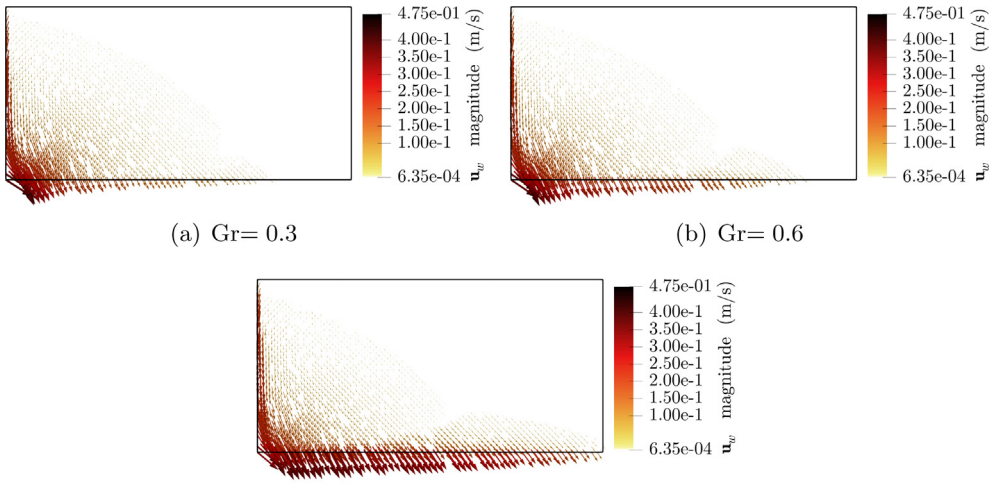

(a) Gr= 0.3 (b) Gr= 0.6

(c) Gr= 1.6

Fig. 24. Two-dimensional pressure-driven flow problem with gravity field: This figure depicts the magnitude and direction of the wetting phase velocity at $t = 600$ s for different gravity numbers.

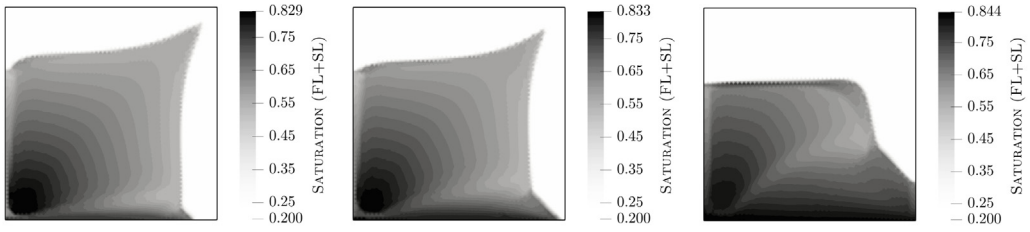

(a) Gr= 0.8 (b) Gr= 1.6 (c) Gr= 4.3

Fig. 25. Quarter five-spot problem with gravity field: This figure depicts saturation contours at $t = 11$ days for different gravity numbers. DG+FL+SL scheme is applied that leads to satisfactory results with respect to maximum principle. By increasing the difference in phases density, gravitational force dominates the viscous force (from left to right). This results in more wetting phase saturation to be deposited at the bottom of domain and hence less non-wetting phase is recovered at the production well.

4.4.2. Quarter five-spot problem

The domain is $\Omega = [0, 1000]^2$ m^2 with permeability of $K = 3 \times 10^{-11}$ everywhere. Capillary pressure and relative permeabilities are defined in Eqs. (4.8) and (4.10), respectively, with entry pressure $P_d = 1000$ Pa, $\theta = 2$ and $R = 0.05$. To address wells, we fix the following parameters: $L_w = 80$ m, $d_w = 80$ m, $\bar{q} = \underline{q} = 9.33 \times 10^{-6}$. The wetting phase density is set to $\rho_w = 1000$ kg/m^3 and the non-wetting phase density takes three different values $\rho_\ell = 925, 850, 600$ kg/m^3, which yields three values for the gravity number Gr= 0.8, 1.6 and 4.3 respectively. The characteristic velocity in Gr estimation is taken as $U \approx 5.5 \times 10^{-5}$ m/s (or 4.8 m/day). Other parameters are the same as in Section 4.3.2. The simulation runs to $T = 11$ days with 750 time steps. Wetting phase saturation contours, wetting phase pressure contours and wetting phase velocity fields are shown in Figs. 25, 26, and 27 respectively. We observe that as the gravity number increases, the inertial forces prevent the saturation to reach the production well. As in the previous section, the discrete solution satisfies the maximum principle. The numerical examples in this section confirm that our proposed numerical method is accurate and robust when gravity dominates.

5. Conclusions

A fully implicit discontinuous Galerkin method is formulated for solving the incompressible two-phase flow equations in porous media. Primary unknowns are the wetting phase pressure and saturation. Nonlinear systems are solved by Newton's method. Post-processing flux is developed and combined with slope limiters to ensure a bound-preserving saturation at each time step. The numerical method is validated on several benchmark problems and it

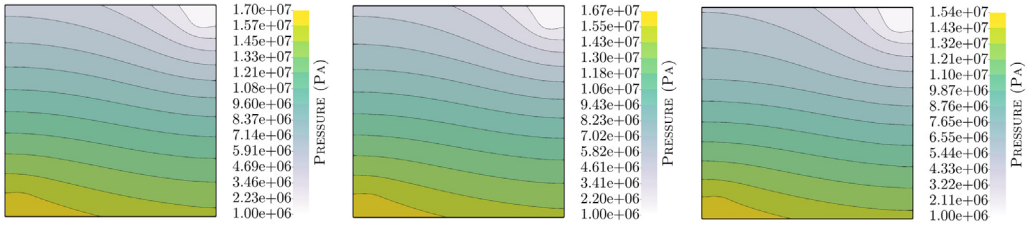

(a) Gr = 0.8 (b) Gr= 1.6 (c) Gr = 4.3

Fig. 26. Quarter five-spot problem with gravity field: This figure shows pressure contours at $t = 11$ days for different gravity numbers. As gravity number increases (from left to right), pressure difference between the injection and the production wells reduces. This is because as the gravitational force dominates, it hinders the wetting phase flow from reaching the production well.

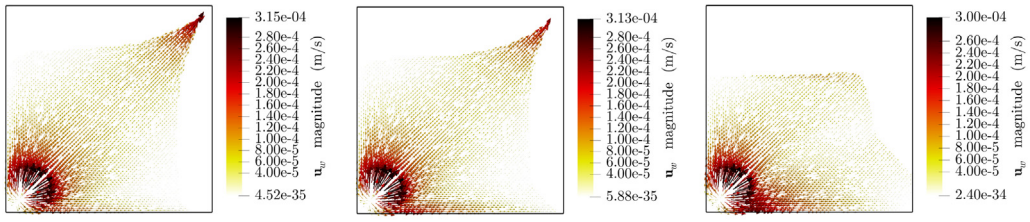

(a) Gr = 0.8 (b) Gr = 1.6 (c) Gr=4.3

Fig. 27. Quarter five-spot problem with gravity field: This figure shows velocity field at $t = 11$ days for different gravity numbers. Increase in gravity number pushes the wetting phase toward the bottom edge and less recovery at the production well, which is also reflected in the decrease in the magnitude of velocities.

is applied to problems where permeability fields are highly varying or where gravitational forces are significant. Flooding of the medium is driven by either pressure boundary conditions or by injection and production wells. The various numerical examples show that the scheme is robust and locally mass conservative. The approximation of the saturation is shown to satisfy the maximum principle both theoretically and computationally.

Declaration of competing interest

The authors declare that they have no known competing financial interests or personal relationships that could have appeared to influence the work reported in this paper.

Acknowledgments

The authors gratefully acknowledge Rustem Zaydullin and Romain De-Loubens for their valuable suggestions and discussions. This work is partially supported by the National Science Foundation, United States of America (NSF-DMS 1913291).

Appendix A. Supplementary data

Supplementary material related to this article can be found online at https://doi.org/10.1016/j.cma.2021.114550.

References

[1] D.W. Peaceman, Fundamentals of Numerical Reservoir Simulation, Vol. 6, Elsevier, 2000.
[2] Khalid. Aziz, Antonin. Settari, Petroleum Reservoir Simulation, 1979, Applied Science Publ. Ltd., London, UK, 1979.
[3] Z. Chen, G. Huan, Y. Ma, Computational Methods for Multiphase Flows in Porous Media, 2, Siam, 2006.
[4] J. Douglas Jr., Finite difference methods for two-phase incompressible flow in porous media, SIAM J. Numer. Anal. 20 (4) (1983) 681–696.
[5] A. Michel, A finite volume scheme for the simulation of two-phase incompressible flow in porous media, SIAM J. Numer. Anal. 41 (2003) 1301–1317.

[6] J. Droniou, Finite volume schemes for diffusion equations: introduction to and review of modern methods, Math. Models Methods Appl. Sci. 24 (08) (2014) 1575–1619.
[7] J.E. Aarnes, S. Krogstad, K.-A. Lie, A hierarchical multiscale method for two-phase flow based upon mixed finite elements and nonuniform coarse grids, Multiscale Model. Simul. 5 (2) (2006) 337–363.
[8] Xiulei. Cao, Koondanibha. Mitra, Error estimates for a mixed finite element discretization of a two-phase porous media flow model with dynamic capillarity, J. Comput. Appl. Math. 353 (2019) 164–178.
[9] M. Wolff, B. Flemisch, R. Helmig, I. Aavatsmark, Treatment of tensorial relative permeabilities with multipoint flux approximation, Int. J. Numer. Anal. Model. 9 (3) (2012).
[10] M. Wolff, Y. Cao, B. Flemisch, R. Helmig, B. Wohlmuth, Multipoint flux approximation L-method in 3D: numerical convergence and application to two-phase flow through porous media, in: Simulation of Flow in Porous Media, De Gruyter, 2013, pp. 39–80.
[11] R. Ahmed, Y. Xie, M.G. Edwards, A cell-centred CVD-MPFA finite volume method for two-phase fluid flow problems with capillary heterogeneity and discontinuity, Transp. Porous Media 127 (1) (2019) 35–52.
[12] W. Klieber, B. Riviere, Adaptive simulations of two-phase flow by discontinuous Galerkin methods, Comput. Methods Appl. Mech. Engrg. 196 (2006) 404–419.
[13] Y. Epshteyn, B. Riviere, Fully implicit discontinuous finite element methods for two-phase flow, Appl. Numer. Math. 57 (4) (2007) 383–401.
[14] Y. Epshteyn, B. Riviere, On the solution of incompressible two-phase flow by a p-version discontinuous Galerkin method, Commun. Numer. Methods. Eng. 22 (2006) 741–751.
[15] A. Ern, I. Mozolevski, L. Schuh, Discontinuous Galerkin approximation of two-phase flows in heterogeneous porous media with discontinuous capillary pressures, Comput. Methods Appl. Mech. Engrg. 199 (23–24) (2010) 1491–1501.
[16] T. Arbogast, M. Juntunen, J. Pool, M.F. Wheeler, A discontinuous Galerkin method for two-phase flow in a porous medium enforcing H(div) velocity and continuous capillary pressure, Comput. Geosci. 17 (6) (2013) 1055–1078.
[17] P. Bastian, A fully-coupled discontinuous Galerkin method for two-phase flow in porous media with discontinuous capillary pressure, Comput. Geosci. 18 (5) (2014) 779–796.
[18] M. Jamei, H. Ghafouri, A novel discontinuous Galerkin model for two-phase flow in porous media using an improved IMPES method, Internat. J. Numer. Methods Heat Fluid Flow 26 (2016) 284–306.
[19] H. Hoteit, A. Firoozabadi, Numerical modeling of two-phase flow in heterogeneous permeable media with different capillarity pressures, Adv. Water Resour. 31 (1) (2008) 56–73.
[20] J. Hou, J. Chen, S. Sun, Z. Chen, Adaptive mixed-hybrid and penalty discontinuous Galerkin method for two-phase flow in heterogeneous media, J. Comput. Appl. Math. 307 (2016) 262–263.
[21] A. Burbeau, P. Sagaut, C.-H. Bruneau, A problem-independent limiter for high-order Runge–Kutta discontinuous Galerkin methods, J. Comput. Phys. 169 (2001) 111–150.
[22] H. Hoteit, Ph. Ackerer, R. Mose, J. Erhel, B. Philippe, New two-dimensional slope limiters for discontinuous Galerkin methods on arbitrary meshes, J. Numer. Meth. Engrg. 61 (2004) 2566–2593.
[23] L. Krivodonova, Limiters for high-order discontinuous Galerkin methods, J. Comput. Phys. 226 (2007) 879–896.
[24] L. Krivodonova, J. Xin, J.-F. Remacle, N. Chevaugeon, J.E. Flaherty, Shock detection and limiting with discontinuous Galerkin methods for hyperbolic conservation laws, Appl. Numer. Math. 48 (2004) 323–338.
[25] D. Kuzmin, A vertex-based hierarchical slope limiter for p-adaptive discontinuous galerkin methods, J. Comput. Appl. Math. 233 (12) (2010) 3077–3085.
[26] D. Kuzmin, Slope limiting for discontinuous Galerkin approximations with a possibly non-orthogonal Taylor basis, Internat. J. Numer. Methods Fluids 71 (2013) 1178–1190.
[27] F. Frank, A. Rupp, D. Kuzmin, Bound-preserving flux limiting schemes for DG discretizations of conservation laws with applications to the cahn–hilliard equation, Comput. Methods Appl. Mech. Engrg. 359 (2019) 112665, http://dx.doi.org/10.1016/j.cma.2019.112665.
[28] D. Kuzmin, Y. Gorb, A flux-corrected transport algorithm for handling the close-packing limit in dense suspensions, J. Comput. Appl. Math. 236 (18) (2012) 4944–4951, http://dx.doi.org/10.1016/j.cam.2011.10.019.
[29] R.H. Brooks, A.T. Corey, Hydraulic Properties of Porous Media, (Ph.D. thesis), Colorado State University. Libraries, 1964.
[30] S. Cherednichenko, C. Frey, G. Ashcroft, On the application of the discontinuous galerkin method to turbomachinery flows, in: In 6th European Congress on Computational Methods in Applied Sciences and Engineering, 2012, pp. 2359–2375.
[31] B.M. Giles, Nonreflecting boundary conditions for euler equation calculations, AIAA J. 28 (12) (1990) 2050–2058.
[32] S. Tamitani, T. Takamatsu, A. Otake, S. Wakao, A. Kameari, Y. Takahashi, Finite-element analysis of magnetic field problem with open boundary using infinite edge element, IEEE Trans. Magn. 47 (5) (2011) 1194–1197.
[33] M. Lenzinger, B. Schweizer, Two-phase flow equations with outflow boundary conditions in the hydrophobic–hydrophilic case, Nonlinear Anal. 73 (4) (2010) 840–853.
[34] D. Kroener, S. Luckhaus, Flow of oil and water in a porous medium, J. Differential Equations 55 (1984) 276–288.
[35] H.W. Alt, E.Di. Benedetto, Nonsteady flow of water and oil through inhomogeneous porous media, Ann. Della Sc. Norm. Super. Di Pisa-Cl. Di Sci. 12 (3) (1985) 335–392.
[36] Y. Epshteyn, B. Riviere, Analysis of hp discontinuous Galerkin methods for incompressible two-phase flow, J. Comput. Appl. Math. 225 (2009) 487–509.
[37] R. Eymard, R. Herbin, A. Michel, Mathematical study of a petroleum-engineering scheme, ESAIM Math. Model. Numer. Anal. 37 (6) (2003) 937–972.
[38] V. Girault, B. Riviere, L. Cappanera, A finite element method for degenerate two-phase flow in porous media, part i: well-posedness, J. Numer. Math. 29 (2) (2021) 81–101a.

[39] V. Girault, B. Riviere, L. Cappanera, A finite element method for degenerate two-phase flow in porous media. part ii: Convergence, J. Numer. Math. (2021b).
[40] S.T. Zalesak, Fully multidimensional flux-corrected transport algorithms for fluids, J. Comput. Phys. 31 (3) (1979) 335–362.
[41] F. Rathgeber, D.A. Ham, L. Mitchell, M. Lange, F. Luporini, A.T.T. McRae, G.T. Bercea, G.R. Markall, P.H.J. Kelly, Firedrake: automating the finite element method by composing abstractions, ACM Trans. Math. Softw. 43 (3) (2016) 24.
[42] A.T.T. McRae, G.T. Bercea, L. Mitchell, D.A. Ham, C.J. Cotter, Automated generation and symbolic manipulation of tensor product finite elements, SIAM J. Sci. Comput. 38 (5) (2016) 25–47.
[43] M. Homolya, D.A. Ham, A parallel edge orientation algorithm for quadrilateral meshes, SIAM J. Sci. Comput. 38 (5) (2016) 48–61.
[44] M. Homolya, L. Mitchell, F. Luporini, D.A. Ham, Tsfc: a structure-preserving form compiler, SIAM J. Sci. Comput. 40 (3) (2018) C401–C428.
[45] M. Homolya, R.C. Kirby, D.A. Ham, Exposing and exploiting structure: optimal code generation for high-order finite element methods, 2017, Available on arXiv:1711.02473.
[46] Zenodo/COFFEE, COFFEE: a compiler for fast expression evaluation, 2020, http://dx.doi.org/10.5281/zenodo.1064647.
[47] Zenodo/FIAT, FIAT: the finite element automated tabulator, 2021, http://dx.doi.org/10.5281/zenodo.1217550.
[48] Zenodo/FInAT, FInAT: a smarter library of finite elements, 2021, http://dx.doi.org/10.5281/zenodo.1135106.
[49] Zenodo/PETSc, PETSC: Portable, extensible toolkit for scientific computation, 2021, http://dx.doi.org/10.5281/zenodo.1217551.
[50] Zenodo/PyOP2, PyOP2: framework for performance-portable parallel computations on unstructured meshes, 2021, http://dx.doi.org/10.5281/zenodo.1251936.
[51] Zenodo/TSFC, TSFC: The two stage form compiler, 2018, http://dx.doi.org/10.5281/zenodo.1251934.
[52] Zenodo/UFL, UFL: the unified form language, 2021, http://dx.doi.org/10.5281/zenodo.1217548.
[53] M.G. Knepley, D.A. Karpeev, Mesh algorithms for PDE with Sieve I: Mesh distribution, Sci. Program. 17 (3) (2009) 215–230.
[54] C. Geuzaine, J.F. Remacle, Gmsh: A 3-d finite element mesh generator with built-in pre-and post-processing facilities, Internat. J. Numer. Methods Engrg. 79 (11) (2009) 1309–1331.
[55] S. Balay, S. Abhyankar, F. Adams M., J. Brown, P. Brune, K. Buschelman, L. Dalcin, V. Eijkhout, W.D. Gropp, D. Kaushik, M.G. Knepley, L.C. McInnes, K. Rupp, B.F. Smith, S. Zampini, H. Zhang, H. Zhang, PETSC Users Manual, Technical Report ANL-95/11 - Revision 3.8,, Argonne National Laboratory, 2017.
[56] S. Balay, S. Abhyankar, M.F. Adams, J. Brown, P. Brune, K. Buschelman, L. Dalcin, V. Eijkhout, W.D. Gropp, D. Kaushik, M.G. Knepley, D.A. May, L.C. McInnes, R.T. Mills, T. Munson, K. Rupp, P. Sanan, B.F. Smith, S. Zampini, H. Zhang, H. Zhang, PETSc web page, 2018.
[57] L.D. Dalcin, R.R. Paz, P.A. Kler, A. Cosimo, Parallel distributed computing using python, Adv. Water Resour. 34 (9) (2011) 1124–1139.
[58] M.A. Crisfield, A faster modified newton-raphson iteration, Comput. Methods Appl. Mech. Engrg. 20 (3) (1979) 267–278.
[59] P.R. Amestoy, I.S. Duff, J. Koster, J.Y. L'Excellent, A fully asynchronous multifrontal solver using distributed dynamic scheduling, SIAM J. Matrix Anal. Appl. 23 (1) (2001) 15–41.
[60] P.R. Amestoy, A. Buttari, J.Y. L'Excellent, T. Mary, Performance and scalability of the block low-rank multifrontal factorization on multicore architectures, ACM Trans. Math. Software 45 (2) (2019) 1–2, 26.
[61] msarrafj/LimitedDG, Codes for a bound-preserving discontinuous galerkin solver for incompressible two-phase flow problem implemented in firedrake project, 2021, https://github.com/msarrafj/LimiterDG.
[62] Zenodo/firedrake, Firedrake: an automated finite element system, 2021, http://dx.doi.org/10.5281/zenodo.1251940.
[63] S.E. Buckley, M. Leverett, et al., Mechanism of fluid displacement in sands, Trans. AIME 146 (01) (1942) 107–116.
[64] Y. Zhang, X. Zhang, C.W. Shu, Maximum-principle-satisfying second order discontinuous galerkin schemes for convection–diffusion equations on triangular meshes, J. Comput. Phys. 234 (2013) 295–316.
[65] X. Zhang, C.W. Shu, Maximum-principle-satisfying and positivity-preserving high-order schemes for conservation laws: survey and new developments, Proc. R. Soc. A Math. Phys. Eng. Sci. 467 (2134) (2011) 2752–2776.
[66] H. Zhang, Y. Guo, W. Li, P.A. Zegeling, Runge-kutta symmetric interior penalty discontinuous galerkin methods for modified buckley-leverett equations, 2018.
[67] F. Fambri, Discontinuous galerkin methods for compressible and incompressible flows on space–time adaptive meshes: toward a novel family of efficient numerical methods for fluid dynamics, Arch. Comput. Methods Eng. 27 (1) (2020) 199–283.
[68] H.H. Welge, et al., A simplified method for computing oil recovery by gas or water drive, J. Pet. Technol. 4 (04) (1952) 91–98.
[69] Z.R. Zhang, T. Tang, An adaptive mesh redistribution algorithm for convection-dominated problems, Commun. Pure Appl. Anal. 1 (3) (2002) 341.
[70] I. Christov, B. Popov, New non-oscillatory central schemes on unstructured triangulations for hyperbolic systems of conservation laws, J. Comput. Phys. 227 (11) (2008) 5736–5757.
[71] R. de Loubens, Construction of High-Order Adaptive Implicit Methods for Reservoir Simulation, (Ph.D. thesis), Department of Energy Resources Engineering Stanford University, 2007.
[72] K.H. Karlsen, K. Brusdal, H.K. Dahle, S. Evje K. A. Lie, The corrected operator splitting approach applied to a nonlinear advection-diffusion problem, Comput. Methods Appl. Mech. Engrg. 167 (3–4) (1998) 239–260.
[73] S. May, M. Berger, Two-dimensional slope limiters for finite volume schemes on non-coordinate-aligned meshes, SIAM J. Sci. Comput. 35 (5) (2013) A2163–A2187.
[74] A. Giuliani, L. Krivodonova, Analysis of slope limiters on unstructured triangular meshes, J. Comput. Phys. 374 (2018) 1–26.
[75] B. Riviere, Discontinuous Galerkin Methods for Solving Elliptic and Parabolic Equations: Theory and Implementation, SIAM, 2008.
[76] M.S. Joshaghani, S.H.S. Joodat, K.B. Nakshatrala, A stabilized mixed discontinuous galerkin formulation for double porosity/permeability model, Comput. Methods Appl. Mech. Engrg. 352 (2019) 508–560.

[77] M. Christie, M. Andrew, M.J. Blunt, Tenth spe comparative solution project: A comparison of upscaling techniques, in: In SPE Reservoir Simulation Symposium, in: Society of Petroleum Engineers, 2001.
[78] A. Riaz, H.A. Tchelepi, Numerical simulation of immiscible two-phase flow in porous media, Phys. Fluids 18 (1) (2006) 014104.
[79] S.M. Hassanizadeh, D.B. Das, Upscaling Multiphase Flow in Porous Media: From Pore to Core and beyond, Springer Berlin, 2005.
[80] H. Tchelepi, L. Dofsky, A. Khalid, A Numerical Simulation Framework for the Design, Management and Optimization of Co2 Sequestration in Subsurface Formations, global climate and energy project (gcep) report,, 2006.